Draft version April 29, 2020
Typeset using LaTeX **preprint** style in AASTeX63

arXiv:2004.13079v1 [astro-ph.GA] 27 Apr 2020

MOSEL: Strong [O III]5007Å Emitting Galaxies at $(3 < z < 4)$ from the ZFOURGE Survey

Kim-Vy H. Tran,[1,2,3] Ben Forrest,[4] Leo Y. Alcorn,[2,5] Tiantian Yuan,[6,3] Themiya Nanayakkara,[7] Jonathan Cohn,[2] Michael Cowley,[8,9] Karl Glazebrook,[6,3] Anshu Gupta,[1,3] Glenn G. Kacprzak,[6,3] Lisa Kewley,[10,3] Ivo Labbé,[6] Casey Papovich,[2] Lee Spitler,[11,3] Caroline M. S. Straatman,[12] Adam Tomczak,[13]

[1]*School of Physics, University of New South Wales, Kensington, Australia*
[2]*George P. and Cynthia W. Mitchell Institute for Fundamental Physics and Astronomy, Department of Physics & Astronomy, Texas A&M University, College Station, TX 77843, USA*
[3]*ARC Centre for Excellence in All-Sky Astrophysics in 3D (ASTRO 3D)*
[4]*Department of Physics & Astronomy, University of California, Riverside, CA 92521, USA*
[5]*LSSTC Data Science Fellow*
[6]*Swinburne University of Technology, Hawthorn, VIC 3122, Australia*
[7]*Leiden Observatory, Leiden University, P.O. Box 9513, NL 2300 RA Leiden, The Netherlands*
[8]*Centre for Astrophysics, University of Southern Queensland, West Street, Toowoomba, QLD 4350, Australia*
[9]*School of Chemistry, Physics and Mechanical Engineering, Queensland University of Technology, Brisbane, QLD 4001, Australia*
[10]*Research School of Astronomy and Astrophysics, The Australian National University, Cotter Road, Weston Creek, ACT 2611, Australia*
[11]*Department of Physics and Astronomy, Faculty of Science and Engineering, Macquarie University, Sydney, NSW 2109, Australia*
[12]*Sterrenkundig Observatorium, Universiteit Gent, Krijgslaan 281 S9, 9000 Gent, Belgium*
[13]*Department of Physics, University of California, Davis, One Shields Ave., Davis, CA 95616*

ABSTRACT

To understand how strong emission line galaxies (ELGs) contribute to the overall growth of galaxies and star formation history of the universe, we target Strong ELGs (SELGs) from the ZFOURGE imaging survey that have blended Hβ+[O III] rest-frame equivalent widths of > 230Å and $2.5 < z_{\rm phot} < 4.0$. Using Keck/MOSFIRE, we measure 49 redshifts for galaxies brighter than $K_s = 25$ mag as part of our Multi-Object Spectroscopic Emission Line (MOSEL) survey. Our spectroscopic success rate is $\sim 53\%$ and $z_{\rm phot}$ uncertainty is $\sigma_z = [\Delta z/(1+z)] = 0.0135$. We confirm 31 ELGs at $3 < z_{\rm spec} < 3.8$ and show that Strong ELGs have spectroscopic rest-frame [O III]5007Å equivalent widths of $100 - 500$Å and tend to be lower mass systems $[\log(M_\star/M_\odot) \sim 8.2 - 9.6]$ compared to more typical star-forming galaxies. The Strong ELGs lie ~ 0.9 dex above the star-forming main-sequence at $z \sim 3.5$ and have high inferred gas fractions of $f_{\rm gas} \gtrsim 60\%$, i.e. the inferred gas masses can easily fuel a starburst to double stellar masses within $\sim 10 - 100$ Myr. Combined with recent results using ZFOURGE, our analysis indicates that 1) strong [O III]5007Å emission signals an early episode of intense stellar growth

Corresponding author: Kim-Vy H. Tran
kimvy.tran@gmail.com

in low mass [$M_\star < 0.1M^\star$] galaxies and 2) many, if not most, galaxies at $z > 3$ go through this starburst phase. If true, low-mass galaxies with strong [O III]5007Å emission ($EW_{rest} > 200$Å) may be an increasingly important source of ionizing UV radiation at $z > 3$.

Keywords: Emission line galaxies (459), Galaxy evolution (594), Galaxy formation (595), Starburst galaxies (1570), Galaxy properties (615), Near infrared astronomy (1093)

1. INTRODUCTION

Hierarchical formation predicts that massive galaxies like our own Milky Way grow through the merger and accretion of smaller systems (Peebles 1970), thus low-mass galaxies that are chemically pristine can provide insight into the early stages of galaxy formation. Although low-mass galaxies are abundant, identifying the ones that are the least chemically evolved via emission lines is difficult due to their rare nature in the local universe. In the past decade, dwarf galaxies with strong [O III]5007Å emission at $z \lesssim 0.3$ (Cardamone et al. 2009; Izotov et al. 2011) have been identified using optical imaging where the large equivalent width of the emission line increases the broadband flux. Valuable insight is gained by measuring, e.g. star formation conditions and ionizing escape fractions (Amorín et al. 2012; Jaskot & Oey 2013; Izotov et al. 2016; Bian et al. 2016; Lofthouse et al. 2017; Izotov et al. 2018), in these local "green pea" galaxies. For example, studies find that strong Hβ+[O III]5007Å emission are ubiquitous in Lyman-break galaxies at $z \sim 7$ (Smit et al. 2014).

A number of studies have now identifed dwarf galaxies ($\log(M_\star/M_\odot) \lesssim 9$) at $0 < z < 2$ with strong [O III]5007Å emission that may bridge local "green peas" to primeval galaxies at $z > 6$. Slit-less near-infrared spectroscopy with the *Hubble Space Telescope* has revealed a population of dwarf galaxies up to $z \sim 2$ with rest-frame [O III]5007Å equivalent widths of $EW_{rest} > 200$Å (e.g. Straughn et al. 2009; van der Wel et al. 2011; Atek et al. 2011). Dedicated ground-based spectroscopic surveys also have identifed Strong Emission Line Galaxies (SELGs) up to $z \sim 1$ (Amorín et al. 2015). These studies suggest that the number density of SELGs increases with redshift (e.g. Maseda et al. 2018). However, quantifying the evolving number density of strong [O III]5007Å emitting galaxies at $z > 1$ requires near-infrared spectroscopy ($\lambda > 1\mu$m), thus only a handful of systems have been confirmed at $z \gtrsim 3$ (de Barros et al. 2016; Nakajima et al. 2016; Amorín et al. 2017).

Once identified, the natural question then is how these strong [O III]5007Å emitting galaxies fit into our existing picture of galaxy formation. The increasing number of Strong ELGs combined with the brief duration of this intense starburst phase ($\lesssim 100$ Myr; Guo et al. 2016; Ceverino et al. 2018) supports a model where galaxies grow through multiple intense starbursts. For starburst systems at $z \gtrsim 3$ with low metallicities, such an episode can signal the initial major growth spurt, i.e. the ELGs with the highest equivalent widths ($EW_{rest} \gtrsim 1000$Å) are "first burst" systems (Cohn et al. 2018). In combination with studies of, *e.g.* Lyman-break galaxies at $z \sim 7$ with strong Hβ+[O III]5007Å emission (Roberts-Borsani et al. 2016), we can use SELGs to test current galaxy formation models that capture the intricate interplay of physics on the sub-kpc scale with the integrated galaxy properties that can be measured at $z > 2$ (Krumholz et al. 2017).

An increasing population of Strong ELGs with redshift also has important implications for cosmic reionization. These vigorously star-forming galaxies have steep UV slopes ($\beta \lesssim -2$) and low metallicities ($Z/Z_\odot \lesssim 0.2$; Forrest et al. 2018; Cohn et al. 2018), i.e. the SELGs may be a tremendous

source of UV photons. By identifying the strong [O III]5007Å emitting galaxies, we can then measure their Lyman-Continuum emission and escape fractions to infer if SELGs at $z > 8$ can generate the UV photons needed to reionize the universe (Ouchi et al. 2009; Mitra et al. 2013; Robertson et al. 2015). Ideally we would track SELGs from $z \sim 0$ to the first galaxies at $z > 8$. However, current near-infrared instruments place a redshift limit of $z \sim 4$ for identifying [O III]5007Å emitters which are the focus of our study.

An effective method to identify galaxies with strong [O III]5007Å emission ($\mathrm{EW_{rest}} > 200$Å) at $z \gtrsim 2$ is to first use deep multi-band photometry to select candidates and then confirm with near-IR spectroscopy. The ELGs with the strongest [O III]5007Å emission tend to be low-mass ($\log(\mathrm{M}_\star/\mathrm{M}_\odot) < 9.5$; e.g. Maseda et al. 2013; Maseda et al. 2014) systems, thus sensitive multi-wavelength imaging is needed to push down in stellar mass to select candidates. Precise photometric redshifts at $z > 1$ also are essential for identifying strong emission line features in the Spectral Energy Distributions (SEDs), and this requires medium-band near-IR imaging. Lastly, only with deep near-IR spectroscopy can the extreme [O III]5007Å nature of these systems be confirmed.

With the advent of deep near-IR imaging surveys and sensitive near-IR spectrographs, we are now able to identify these strong [O III]5007Å emitting galaxies at $z \sim 3-4$. Our method is similar to studies that couple near-IR imaging and near-IR spectroscopy to identify galaxies with strong equivalent widths at $z \sim 1-2$, e.g. `3D-HST` (Maseda et al. 2013; Maseda et al. 2014, 2018). First we use the `ZFOURGE` survey that measures precise photometric redshifts to $\sim 70,000$ objects by combining deep imaging with medium-band near-IR filters $J_1 J_2 J_3 H_s H_l K_s$ and public multi-wavelength observations (redshift uncertainties of $\sigma_z \sim 1.6\%$; Straatman et al. 2016). At $z \sim 3$, the `ZFOURGE` survey is 80% mass-complete to $\log(\mathrm{M}_\star/\mathrm{M}_\odot) \sim 9.5$ and measures star formation rates down to $\sim 5\ \mathrm{M}_\odot\ \mathrm{yr}^{-1}$ (Tomczak et al. 2016).

With photometry spanning observed UV to mid/far-IR, we then construct composite SEDs that are defined by the underlying galaxy populations (Kriek et al. 2011; Forrest et al. 2016). In our analysis of `ZFOURGE` galaxies at $2.5 < z_{\mathrm{phot}} < 4.0$, we discovered a population of ~ 80 galaxies with blended rest-frame Hβ+[O III] equivalent widths in excess of ~ 800Å (Forrest et al. 2017). In comparison, there are only ~ 14 galaxies with such extreme Hβ+[O III] at $1 < z < 3$ (Forrest et al. 2018). The rapid increase in the number density of the extreme Hβ+[O III] emitting galaxies from $z \sim 2$ to $z \sim 3.5$ suggests potentially explosive growth at higher redshift (see also van der Wel et al. 2011).

To spectroscopically confirm the Hβ+[O III] emitting galaxies identified in `ZFOURGE`, we introduce our Multi-Object Spectroscopic Emission Line (`MOSEL`[1]) survey. In this paper, we focus on Emission Line Galaxies (ELGs) at $2.5 < z_{\mathrm{phot}} < 4.0$ to measure their redshifts and rest-frame [O III]5007Å equivalent widths and line-widths. We combine our spectroscopic measurements with physical properties obtained from deep multi-band imaging to infer gas fractions and virial masses, and test disk formation models.

By identifying Strong ELGs up to $z \sim 4$ (Forrest et al. 2017, 2018), `MOSEL` complements existing emission line searches conducted with the *Hubble Space Telescope*. Due to the wavelength ranges of the WFC3 and ACS grisms, blind spectroscopic surveys such as `3D-HST` (Momcheva et al. 2016), `WISP` (Atek et al. 2011), and `PEARS` (Straughn et al. 2008) are limited to SELGs at $z \lesssim 2.3$. Our medium-band NIR imaging from `ZFOURGE` combined with public legacy datasets enables us to reach

[1] Mosel is also one of the 13 official German wine regions (Weinbaugebiete) and known for Riesling and Pinot Noir.

comparable stellar masses as the blind spectroscopic surveys ($\log(M_\star/M_\odot)\sim 8.5$ at $z\sim 1$; Straatman et al. 2016). At $z\sim 3-4$, we also span comparable ranges in rest-frame equivalent width ($\gtrsim$ 200Å) and spectral line flux ($\sim 1-2\times 10^{-17}$erg s^{-1} cm^{-2} Å^{-1}) as the lower redshift studies.

In our analysis, we use AB magnitudes and the galaxy parameters measured by Forrest et al. (2017, 2018) for the ZFOURGE data-set. FAST (Kriek et al. 2009) is used to fit the SEDs assuming a Chabrier Initial Mass Function and an SED library with 1/5 solar metallicity and emission lines (see Salmon et al. 2015; Forrest et al. 2018). We assume $\Omega_{\rm m}=0.3$, Ω_Λ=0.7, $H_0=70$ km s^{-1} Mpc^{-1}, and a flat Universe; the corresponding angular scale at $z=3.0$ is 7.7 kpc per arcsec.

2. DATA & METHODS

2.1. *Selecting Emission Line Galaxies*

The following summarizes the ZFOURGE observations we used to measure photometric redshifts and galaxy properties as well as to generate the composite SEDs. For complete descriptions of the data products used here, we refer the reader to the ZFOURGE survey paper by Straatman et al. (2016) and analysis of star formation rates by Tomczak et al. (2016).

2.1.1. ZFOURGE *Imaging Catalogs*

We use the deep near-IR imaging from the FourStar Galaxy Evolution survey (ZFOURGE; Straatman et al. 2016) obtained with the FourStar imager (Persson et al. 2013) on the Magellan Telescope of three legacy fields: CDFS (Giacconi et al. 2002), COSMOS (Scoville et al. 2007), and UDS (Lawrence et al. 2007). ZFOURGE divides the J-band filter into J_1, J_2, and J_3 and the H-band filter into H_s and H_l; ZFOURGE also obtains deep K_s imaging that is used as the detection image. In combination with existing multi-wavelength observations, ZFOURGE provides high precision photometric redshifts with σ_z= 0.016 (Straatman et al. 2016) for over 70,000 objects; the redshift precision is confirmed by the ZFIRE spectroscopic survey (Nanayakkara et al. 2016).

We incorporate HST imaging from CANDELS (Grogin et al. 2011; Koekemoer et al. 2011) spanning 0.3μm to 1.6μm to measure photometry and galaxy properties. We also use *Spitzer*/IRAC (all four channels) and MIPS data (24μm) for the CDFS, COSMOS, and UDS fields (GOODS-S: PI Dickinson, COSMOS: PI Scoville, UDS: PI Dunlop), and 100 and 160μm for CDFS. For CDFS only, we include public *Herschel*/PACS data (Elbaz et al. 2011). Total star formation rates are calculated by combining the UV and IR contributions; see Tomczak et al. (2016, §2) for a detailed description.

2.1.2. *Candidate Emission Line Galaxies at* $2.5<z_{\rm phot}<4.0$

ZFOURGE is particularly sensitive to emission line galaxies at $2.5<z_{\rm phot}<4.0$ because Hβ+[O III] emission falls in the deep K_s imaging. To identify galaxies with the strongest emission lines, we use the composite SEDs generated by Forrest et al. (2017). From testing multiple fitting methods, Forrest et al. (2018, §4.5) show that restframe equivalent widths down to $\sim$ 20Å can be recovered from the composite SEDs; in the case of Hβ+[O III], the detection threshold applies to the blended EW$_{\rm rest}$.

To summarize, we iteratively select the *primary galaxies* with the largest number of *analog galaxies* based on the similarity of 22 rest-frame UVOIR colors ($b<0.05$, from Kriek et al. 2011; Forrest et al. 2016) to collectively form separate *composite groups*. Observed photometry from analog galaxies in each composite group are then de-redshifted, normalized to a common flux scale, and combined to build a composite SED, essentially a low resolution ($R\sim 40$) spectrum.

We focus on the two composite SEDs from Forrest et al. (2017, 2018) with the steepest UV slope and strongest blended Hβ+[O III] emission. We adopt an admittedly arbitrary definition and refer to these emission line galaxies as *Strong* (SELG). In our analysis, we refer to the following types of galaxies:

- Star-Forming Galaxy (SFG): composite SEDs with rest-frame Hβ+[O III] equivalent widths of < 230Å
- Strong Emission Line Galaxy (SELG): the combined sample of 278 galaxies in S_1ELG and S_2ELG.
- S_1ELG: the 60 galaxies grouped in the the composite SED with rest-frame Hβ+[O III] equivalent width of > 800Å
- S_2ELG: the 218 galaxies grouped in the the composite SED with rest-frameHβ+[O III] equivalent width of $230 - 800$Å

Across the three ZFOURGE fields, we identify a total of 278 candidate Strong ELGs from the ZFOURGE composite SEDs, the majority of which are in CDF-S (Forrest et al. 2017). Except where noted, we use the combined sample of SELGs=(S_1ELG+S_2ELG) . We exclude Active Galactic Nuclei (AGN) identified by Cowley et al. (2016) using multi-wavelength diagnostics; we discuss this in more detail in §3.7.

2.2. *Keck/MOSFIRE Spectroscopy*

2.2.1. *Observations*

We used MOSFIRE (McLean et al. 2012) on Keck I (project code Z245, PI Kewley) on 12 and 13 February 2017. We observed 5 masks in COSMOS and 1 mask in CDFS. To measure Hβ+[O III] at $z \sim 3$, we used the K-band with wavelength range of $1.93 - 2.38\mu$m and spectral dispersion of 2.17 Å/pixel. We used an AB dither pattern with 1.5 arcsecond nod and integrated each mask for a total on-sky time of 96 minutes (110 minutes clock time); seeing ranged from $0.7 - 1$ arcsec.

In the six MOSFIRE masks, we targeted a total of 105 galaxies at $0.9 < z_{\rm phot} < 4.8$ where the highest priority targets were the 38 Strong ELGs candidates at $2.5 < z_{\rm phot} < 4.0$. The remaining targets (67) primarily were star-forming galaxies at $2 < z_{\rm phot} < 4$. Each mask included a flux monitor star to anchor the spectro-photometric calibrations. We follow the same reduction pipeline as in our ZFIRE survey (Tran et al. 2015; Nanayakkara et al. 2016; Tran et al. 2017) and estimate a 3σ line-flux limit in the MOSFIRE K-band of $\sim 3 \times 10^{-18}$ erg s^{-1} cm^{-2}. Note that the angular sizes of the galaxies are comparable to or smaller than the slit-width of $0.7''$ (Fig. 7), *i.e.* there should be no significant systematic error such as slit-loss due to the spectro-photometric calibration.

2.2.2. *Spectroscopic Redshifts*

Of the 105 galaxies targeted with MOSFIRE, we measure spectroscopic redshifts for 49 ($2.091 < z_{\rm spec} < 4.751$; Fig. 1). Considering only the 89 targeted galaxies with photometric redshifts in the same range, i.e. galaxies where [O III] and Hα fall in the K-band, our success rate is $\sim 53\%$. The 49 galaxies with spectroscopic redshifts have K_s magnitudes brighter than 25 and quality flag of $Q_{\rm z} \geq 2.5$. In our analysis, $Q_{\rm z} \geq 2.5$ means that the spectral line emission matches the ZFOURGE

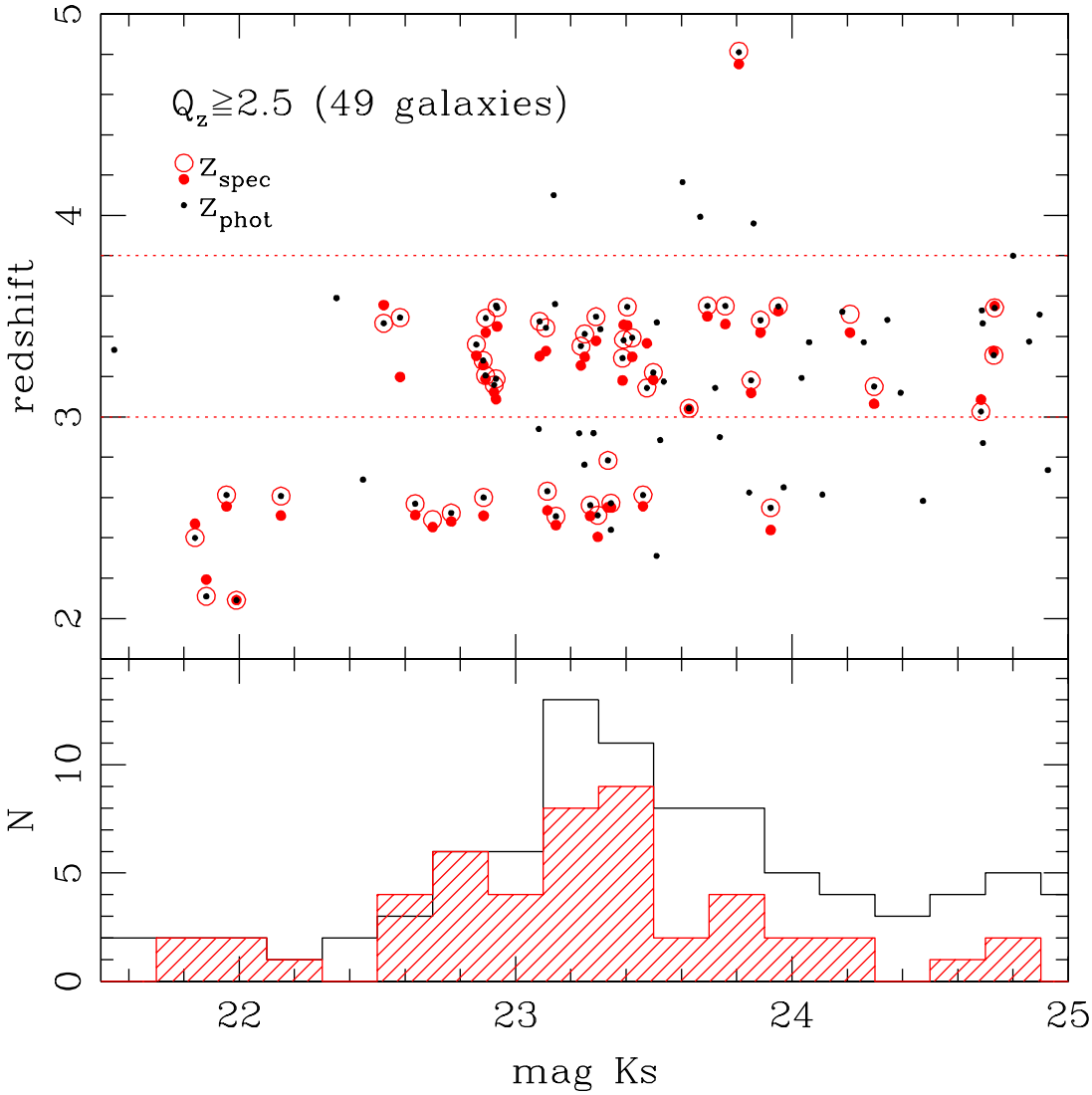

Figure 1. We compare the photometric redshifts (top) and K_s magnitudes (bottom) of the 95 targeted galaxies (small filled black circles & open black histograms) to the 49 galaxies with spectroscopic redshifts (vertical pairs of large filled+open red circles & hashed red histograms). The two samples are likely drawn from the same parent population: KS tests comparing the $z_{\rm phot}$ and K_s magnitudes of the 49 galaxies with $z_{\rm spec}$ to that of the targeted sample measure probabilities of 14% and 6% respectively. The median $z_{\rm spec}$ of these 49 galaxies is only $\sim 1\%$ lower than their median $z_{\rm phot}$ (3.19 vs. 3.22). Our analysis focuses on the 31 spectroscopically confirmed galaxies at $3 < z_{\rm spec} < 3.8$ where Hβ+[O III] fall in the MOSFIRE K-band (top panel, horizontal dashed lines).

photometric redshift or there are two spectral lines with the same redshift (for all definitions of $Q_{\rm z}$, see Nanayakkara et al. 2016).

On average, $z_{\rm phot}$ is $\sim$ 0.054 higher than $z_{\rm spec}$ (Fig. 1) and the corresponding uncertainty is σ_z=[$\Delta z/(1+z)$] = 0.0135. The largest outliers have $\Delta z \sim 0.3$ and $\sigma_z \sim 0.07$. A two-sample Kolmogrov-Smirnov test shows the probability that the spectroscopically confirmed sample and the targeted sample are drawn from the same parent $z_{\rm phot}$ distribution to be 3.6%, *i.e.* the two distribu-

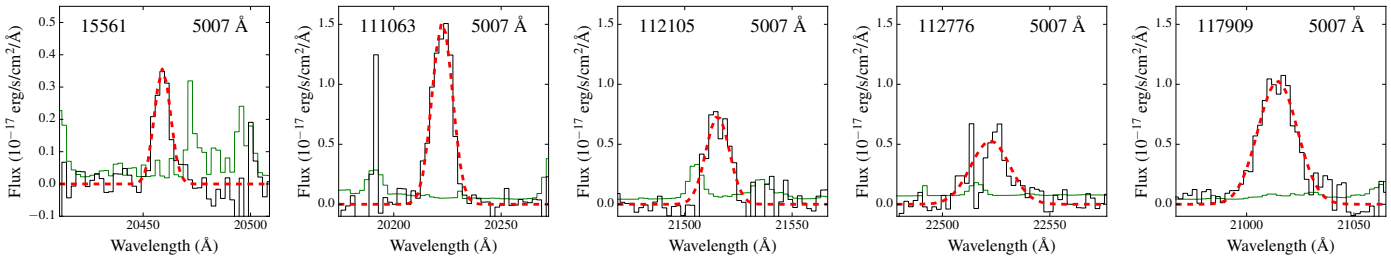

CDFS COSMOS COSMOS COSMOS COSMOS

Figure 2. Example of fits to the MOSFIRE spectra (§2.2.3) showing the observed 1D spectrum (black), the 1D error spectrum (green), and the 1D Gaussian fit (red dashed curve).

tions are different at the 2σ level. The spectroscopically confirmed sample also is ~ 0.25 magnitudes brighter with a K-S probability of being drawn from the same parent K_s distribution as the targeted sample of 15%.

Of the 13 targeted S_1ELG that were grouped in the composite SED with the highest Hβ+[O III] emission (EW_{rest}> 800Å), two were lost due to mechanical problems with configuring the mask and two had no measured redshift. The median redshift of the 9 confirmed ELGs is z_{spec}=3.189 compared to their median z_{phot}=3.207. The corresponding uncertainty of σ_z=0.42% is even lower than that of our ZFIRE survey which targeted a broader selection of galaxies at $z \sim 2$ (Tran et al. 2015; Nanayakkara et al. 2016). Note also that the largest outliers are $\Delta z \sim 0.1$ which is a factor of three smaller compared to the SFGs ($\Delta z \sim 0.3$). In our analysis, we focus on the 8 ELGs at $3 < z_{spec} < 3.8$ and exclude the ELG at z_{spec}= 2.549 (ID 4791).

Of the 25 targeted S_2ELG that were grouped in the composite SED with the second highest Hβ+[O III] emission (230 <EW_{rest}< 800Å), 13 were spectroscopically confirmed with a median redshift of z_{spec}=3.327 compared to their median z_{phot}=3.41. The corresponding uncertainty of σ_z=1.9% for the S_2ELG is larger than that of the S_1ELG and more typical of the ZFOURGE survey as a whole (Straatman et al. 2016; Nanayakkara et al. 2016). All 13 have redshifts of $3 < z_{spec} < 3.8$.

Of the remaining 67 galaxies targeted with MOSFIRE, 28 have spectroscopic redshifts (Fig. 1) with a median redshift of z_{spec}=2.551 compared to their median z_{phot}=2.612. In our analysis, we focus on the 10 SFGs at $3 < z_{spec} < 3.8$, i.e. we exclude the 17 galaxies at z_{spec}< 2.6 and the one galaxy at z_{spec}= 4.815. We note that due to decreasing throughput of the near-IR arrays at $\lambda \gtrsim 2.2\mu$m, the redshift cut-off is effectively $z \sim 3.6$ except for objects with the strongest [O III]5007Å emission.

2.2.3. *Measuring [O III]5007Å Spectral Line Emission*

Following Alcorn et al. (2016, 2018), we first extract a 1D spectrum from an aperture defined by the 1σ Gaussian width of the [O III]5007Å emission line along the spatial direction (Fig. 2). To determine the [OIII]5007Å line flux, we integrate the best-fit Gaussian centered on the line emission along the wavelength direction using the 3σ range; all line-fits are visually inspected for quality control. We subtract in quadrature the instrumental broadening from the measured line-width and then convert to an integrated velocity dispersion (σ_{int}) using the galaxy's measured redshift. Errors in σ_{int} are estimated by adding sky noise to the observed spectrum and refitting 1000 times.

2.2.4. *Determining [O III]5007Å Equivalent Width*

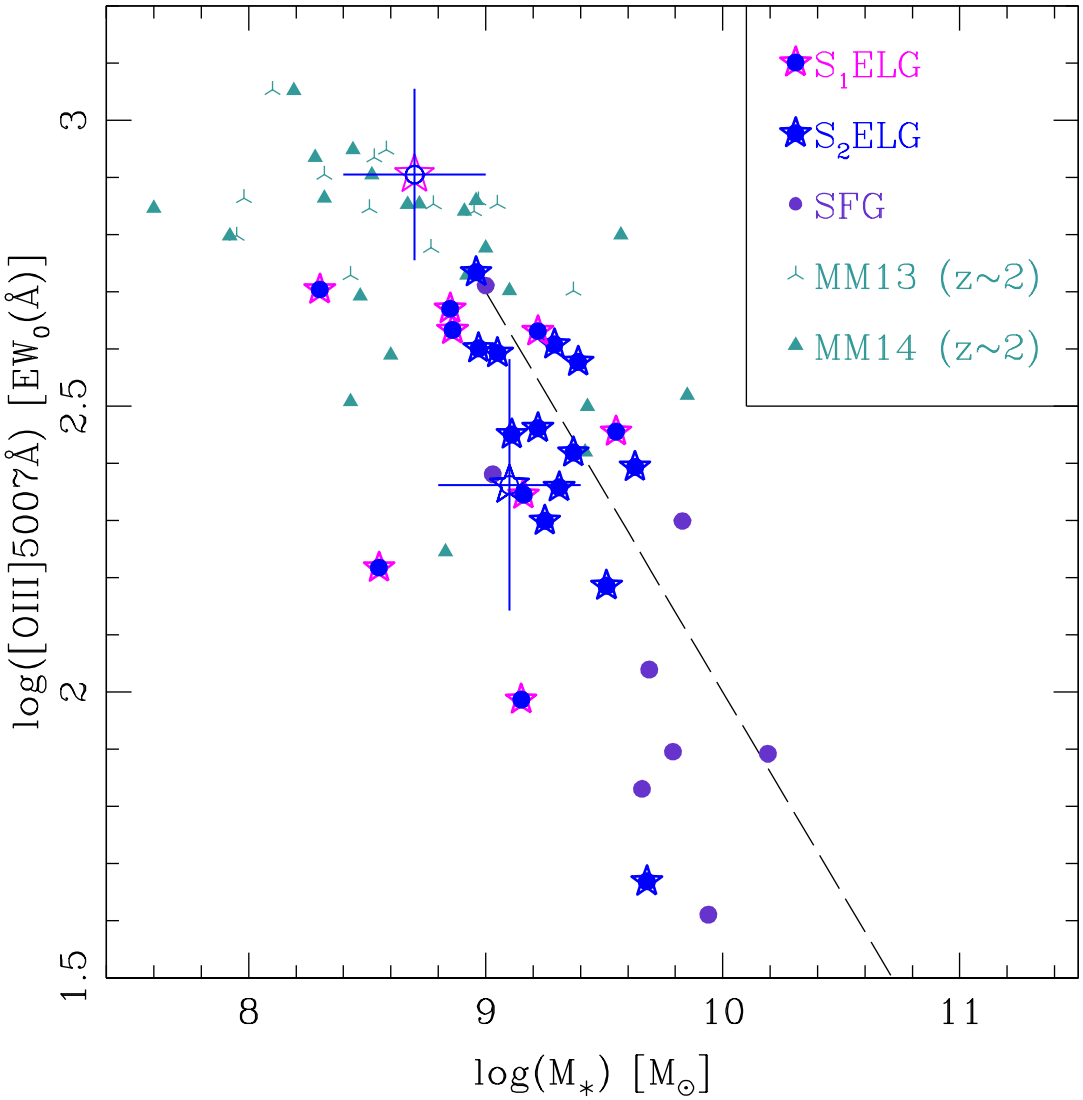

Figure 3. Spectroscopic rest-frame [O III]5007Å equivalent widths for confirmed Emission Line Galaxies (ELGs) at $3 < z_{\rm spec} < 3.8$; typical uncertainties in stellar mass are ~ 2 (Forrest et al. 2018). The symbols denote galaxy classifications as defined by the Composite SEDs, i.e. from photometry only, and the large open stars show the rest-frame blended Hβ+[O III] equivalent width *as measured from the two composite SEDs with the strongest emission* from Forrest et al. (2017). Shown are: 1) S_1ELG with blended rest-frame Hβ+[O III] EW$_{\rm rest}$> 800 Å as measured from their Composite SED; 2) S_2ELG with blended rest-frame Hβ+[O III] EW$_{\rm rest}\sim 230-800$ Å; and 3) more typical star-forming galaxies with blended rest-frame Hβ+[O III] EW$_{\rm rest}$< 230 Å. For comparison, Strong ELGs at $1 < z < 3$ selected with `3D-HST` (Maseda et al. 2013; Maseda et al. 2014) are shown in cyan; the spectral resolution and flux limit of the grism observations selects ELGs with the highest [O III]5007Å EWs. The dashed line shows the average relationship between [O III]5007Å EW$_{\rm obs}$ and stellar mass from MOSDEF for galaxies at $z \sim 2$ (Reddy et al. 2018).

To measure [O III]5007Å equivalent widths, we require both line and continuum flux. However, most of the ELGs are too faint to directly measure their continua from the MOSFIRE spectroscopy. We use the method described in Nanayakkara et al. (2017) that combines our spectro-photometrically calibrated [O III]5007Å line fluxes with the deep continuum photometry from ZFOURGE (Straatman et al. 2016). Because the ZFOURGE photometry provides a better measurement of the faint continuum relative to the spectroscopy, the primary source of uncertainty is thus due to systematic error of the spectro-photometric calibration, and this uncertainty is of order $\sim 10-20\%$ for continuum-detected galaxies (Nanayakkara et al. 2016). Note that given the galaxy sizes are comparable to or smaller than the slit-width of (Fig. 7), the systematic error due to the spectro-photometric calibration is not significant.

To determine the continuum for each ELG, we use the FAST fits (Kriek et al. 2009) from Forrest et al. (2017, 2018) that include a template library with strong emission lines. As we show in both Cohn et al. (2018) and Forrest et al. (2018), the stellar masses for low-mass galaxies ($\log(M_\star/M_\odot) \lesssim 10$) can be overestimated by $\sim 0.5-0.7$ dex if strong emission lines are not included in the SED modeling. The emission lines are from Salmon et al. (2015) who couple the photoionization code Cloudy (Ferland et al. 2013) with BC03 simple stellar populations (Bruzual & Charlot 2003) as the ionizing source to generate nebular emission models.

Because both star formation rate and stellar mass depend on the adopted stellar metallicity, SED fits are generated for solar ($Z = 0.02$) and subsolar ($Z = 0.004$) values. The strong emission lines indicate the ELGs have gas metallicities lower than solar, thus we use the subsolar stellar metallicity fits ($Z = 0.004$; see also Cohn et al. 2018). However, we stress that the value adopted for the metallicity does not change the measured value for the continuum nor the measured $\mathrm{EW_{rest}}$, only how we interpret the measurements.

We calculate the observed frame continuum on the blue and red side of the Hβ+[O III] lines by using tophat filters (width of 150Å) centered at 4675Å and 5200Å on the best-fit FAST SED. We then divide the observed [O III]5007Å line flux by the average observed continuum and the galaxy redshift.

$$\mathrm{EW_{rest}}(5007) = \frac{f_{\mathrm{line}}(5007)}{[(f_{\mathrm{cont}}(4675) + f_{\mathrm{cont}}(5200)]/2} \left(\frac{1}{1+z}\right) \tag{1}$$

For a line flux of 3×10^{-18} erg s^{-1} cm^{-2} and continuum flux of 5×10^{-20} erg s^{-1} cm^{-2} Å^{-1} (approximately K_s magnitude of 24.0), the observed equivalent width is 60Å; for a galaxy at z_{spec}=3.0, the corresponding rest-frame equivalent width is $\mathrm{EW_{rest}}$= 15Å. For comparison, the lowest values we measure for the spectral rest-frame equivalent widths using MOSFIRE are $\sim$ 20Å (Table 2). We note that Forrest et al. (2018, §4.5) estimated rest-frame $\mathrm{EW_{rest}}$ down to $\sim$ 20Å can be measured from the composite SEDs.

For reference, the 3D-HST survey quotes a 3σ emission line flux limit for point sources of 1.5×10^{-17} erg s^{-1} cm^{-2} (Momcheva et al. 2016). Assuming the same continuum flux level, their limit corresponds to an observed equivalent width of 300Å, i.e. approximately five times higher than MOSEL.

3. RESULTS

In our analysis, we focus on the 31 galaxies that are spectroscopically confirmed to be at $3 < z_{\mathrm{spec}} < 3.8$ (Fig. 1). We measure the [O III]5007Å emission for these galaxies with our K-band spectroscopy

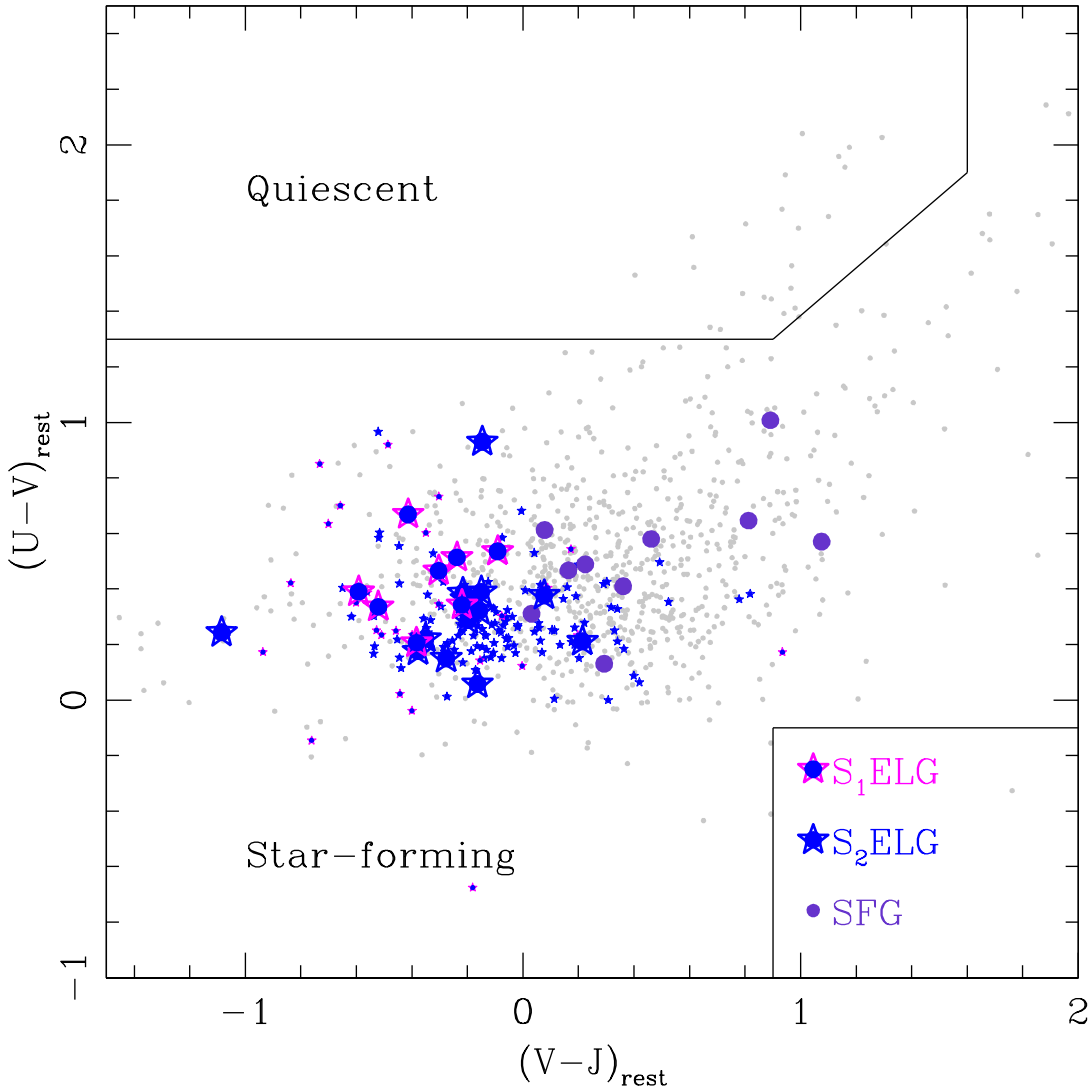

Figure 4. Rest-frame UVJ colors of ZFOURGE galaxies at 2.5 $<z_{\rm phot}<$ 4.0 identified using Composite SEDs, i.e. with photometry only (Forrest et al. 2017). The Strong ELGs are galaxies from the two composite SEDs with the strongest blended Hβ+[O III] emission (S_1ELG and S_2ELG; small stars). Larger symbols show the 31 spectroscopically confirmed galaxies at $3 < z_{\rm spec} < 3.8$ that include more typical star-forming galaxies (purple). Typical uncertainties in rest-frame colors are not significant (< 0.1), i.e. comparable to the symbol sizes. Because of their strong Hβ+[O III] emission, SELGs (stars) tend to have $(V - J) < 0$ colors and are offset relative to the broader ZFOURGE population at 2.5 $<z_{\rm phot}<$ 4.0 (gray circles). None of the MOSEL galaxies are dusty as defined using the criterion from Spitler et al. (2014) of $(V - J)\geq 1.2$.

(Fig. 2). We combine our spectral measurements with deep photometry from ZFOURGE to measure continuum properties and use galaxy sizes from van der Wel et al. (2012). Although the $L_{\rm UV+IR}$-based SF rates from Tomczak et al. (2016) based on solar metallicity models are robust to significant flux from line emission, the stellar masses can be overestimated by as much as a factor of ~ 2 (e.g. Forrest et al. 2018; Cohn et al. 2018). For these galaxies, we use stellar masses determined using

updated FAST fits that include an SED template with strong emission lines and 1/5 solar metallicity ($Z = 0.004$; Forrest et al. 2018).

3.1. *Strong [O III]5007Å Emission*

With our MOSFIRE spectroscopy and deep multi-band imaging, we estimate rest-frame [O III]5007Å equivalent widths using the hybrid method described in §2.2.4. Our spectroscopically confirmed Strong ELGs span similar ranges with [O III]5007Å $\mathrm{EW_{rest}} \sim 100 - 500$Å (Fig. 3). These ranges are consistent with the large blended Hβ+[O III] equivalent widths ($\mathrm{EW_{rest}} \gtrsim 200$Å) measured from their composite SEDs (Forrest et al. 2017, 2018).

The Strong ELGs at $3 < z_{\mathrm{spec}} < 3.8$ show a trend of decreasing [O III]5007Å equivalent width with increasing stellar mass that is also observed in SELGs at $z \sim 2$ (Fig. 3; Maseda et al. 2014). The significant overlap between $\mathrm{S_1}$ELG and $\mathrm{S_2}$ELG indicates that the two are not distinctly different populations. Note that the SELGs at $z \sim 2$ include systems with $\log(\mathrm{M_\star/M_\odot}) \sim 8$ while our $z \sim 3-4$ SELGs have $\log(\mathrm{M_\star/M_\odot}) \gtrsim 8.5$ due to sensitivity limits.

The more typical star-forming galaxies (Hβ+[O III]$\lesssim 230$Å) at $3 < z_{\mathrm{spec}} < 3.8$ have larger stellar masses ($\log(\mathrm{M_\star/M_\odot}) \gtrsim 10$) and lower rest-frame [O III]5007Å equivalent widths ($\mathrm{EW_{rest}} \sim 40 - 250$Å; Fig. 3). This reflects the larger contribution of stellar continuum light, i.e. for two galaxies with the same [O III]5007Å line-flux, the galaxy with the brighter continuum will have a lower equivalent width. Our results confirm that selecting Strong ELGs from the ZFOURGE photometry is effective at identifying galaxies with the largest [O III]5007Å equivalent widths.

For the $\mathrm{S_1}$ELG, the [O III]5007Å $\mathrm{EW_{rest}}$ values determined using the line fluxes obtained with MOSFIRE (see §2.2.4) tend to be lower than the $\mathrm{EW_{rest}}$ value estimated from the composite SED (Fig. 3). The offset is likely driven by how the continuum and emission lines are combined to generate the template used to fit the composite SEDs. For example, underestimating the continuum will increase the inferred EW. We refer the reader to Forrest et al. (2017) who test three fitting methods on the composite SEDs of the strongest ELGs.

3.2. *Rest-frame UVJ Colors*

With the ZFOURGE rest-frame wavelength coverage of $0.08 - 7\mu$m for each galaxy, we measure continuum properties including rest-frame UVJ colors from the individual SEDs (Tomczak et al. 2014; Straatman et al. 2016). ZFOURGE galaxies at $2.5 < z_{\mathrm{phot}} < 4.0$ span the range in UVJ colors (Fig. 4) to include dusty and quiescent systems, but most lie in the star-forming region of the UVJ diagram (see also Straatman et al. 2016). The "typical" star-forming galaxies in our spectroscopic sample have $(V-J) \lesssim 0.5$ that are values consistent with low amounts of reddening ($\mathrm{A_V} < 0.5$; Forrest et al. 2016). None of the spectroscopically confirmed galaxies are dusty as defined using the criterion from Spitler et al. (2014) of $(V-J) \geq 1.2$.

In contrast, the Strong ELGs are offset towards bluer $(V-J)$ colors (Fig. 4). Their strong Hβ+[O III] emission significantly boosts their V-band fluxes to produce rest-frame values of $(V-J) < 0$; this is particularly striking for the $\mathrm{S_1}$ELG where virtually all have $(V-J) < 0$. Such blue UVJ colors and non-detections in the far-IR indicate that these ELGs are essentially dust-free systems. The relative distributions of the $\mathrm{S_1}$ELG and $\mathrm{S_2}$ELG in the UVJ diagram suggests a continuum of phases where age and dust content increases from the Strong ELGs to the more typical star-forming galaxies, e.g. Lyman-Break Galaxies.

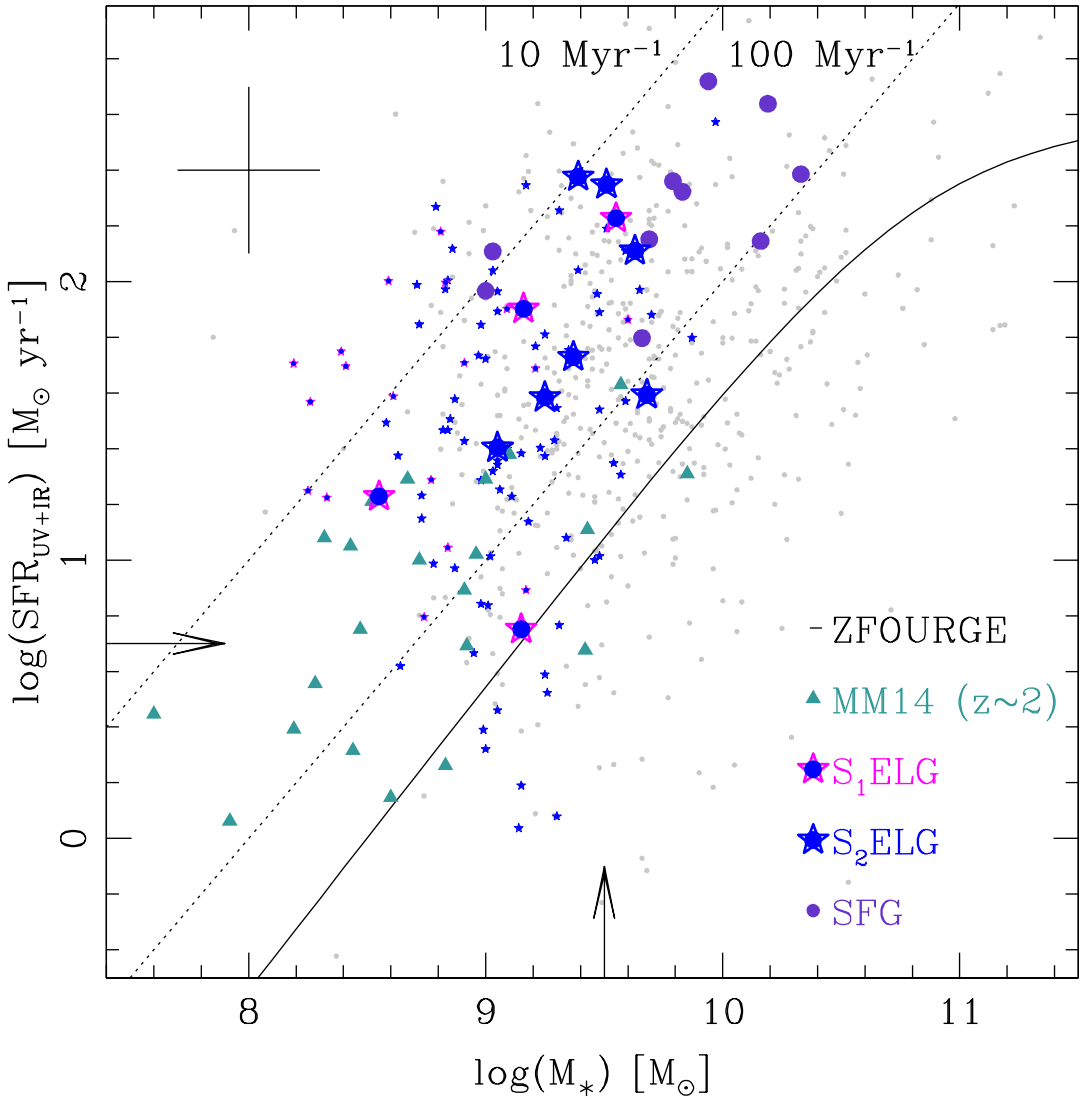

Figure 5. Hβ+[O III] emitting galaxies tend to lie ~ 0.9 dex above the star-forming main sequence (SFMS) at $z = 3.5$ (solid curve based on stacked star formation rates; Tomczak et al. 2016); symbols are as in Fig. 4 and illustrative errorbars correspond to a factor of two uncertainty in stellar mass and star formation rate. Arrows denote the completeness limits at $z \sim 3.5$ from ZFOURGE (Tomczak et al. 2016). Total star formation rates are based on ZFOURGE (UV+IR) fluxes, and here we plot only the galaxies that are individually detected in the IR. The Strong Hβ+[O III]-emitters with $z_{\rm spec}$ (large stars) have the same distribution as their respective $z_{\rm phot}$ samples (small stars). The diagonal dotted lines denote mass-doubling timescales of 10 and 100 Myr. Strong ELGs at $1.4 < z < 2.3$ (filled triangles; Maseda et al. 2014) also tend to lie above the SFMS.

3.3. *Star-Formation Rate vs. Stellar Mass*

The Strong ELGs tend to be lower mass systems [$\log(M_\star/M_\odot) \sim 8.2 - 9.6$] compared to more typical star-forming galaxies (Fig. 3). At $z \sim 3$, the $\log(M^\star)$ for the stellar luminosity function from ZFOURGE is ~ 10.7 (Tomczak et al. 2014). In comparison, the SELGs have stellar masses of only $M_\star \sim (0.003 - 0.08)\ M^\star$.

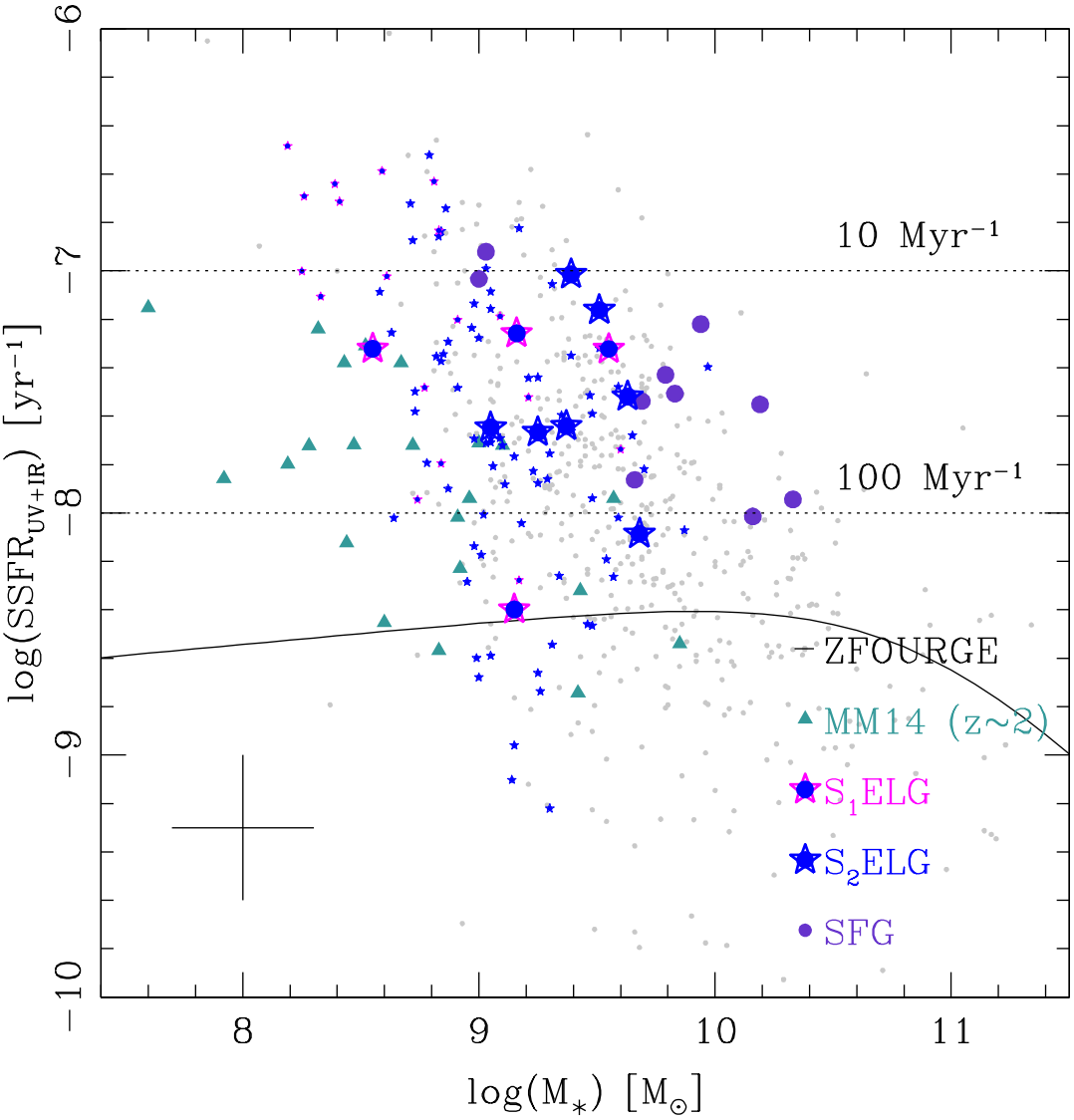

Figure 6. The starburst nature of the Hβ+[O III] emitting galaxies is underlined by their high specific Star Formation Rates (SSFR) defined as their (UV+IR) SFRs divided by their stellar masses. Symbols are as in Fig. 5 and included for comparison is the SSFR-M$_\star$ at $z = 3.5$ from Tomczak et al. (2016); illustrative errorbars correspond to a factor of two uncertainty in stellar mass and specific star formation rate. Most of the Strong ELGs (stars) have mass-doubling times of < 100 Myr with several systems at < 10 Myr (dotted horizontal lines). Included for comparison are the ELGs at $1 < z < 3$ from Maseda et al. (2014) that all have mass-doubling times > 10 Myr and tend to be low-mass ($\log(M_\star/M_\odot) < 9$). As SELGs grow in stellar mass and evolve into more typical SFGs, they move diagonally from the upper left to the bottom right.

Figure 5 shows the star formation rate to stellar mass (SFR-M$_\star$) for the galaxies in our sample with measured (UV+IR) star formation rates from `ZFOURGE` (Tomczak et al. 2016). Although all of our galaxies have measured UV fluxes, many have negative IR fluxes due to the SED fitting method (see §2.5 of Tomczak et al. 2016) and thus 13 of the 31 galaxies have negative (unphysical) total SFRs and are excluded from the SFR-M$_\star$ analysis. Also, note that our 3σ line-flux limit in the MOSFIRE K-band is $\sim 3 \times 10^{-18}$ erg s^{-1} cm^{-2} (see also Tran et al. 2017).

Of the 18 ELGs with positive (UV+IR) SFRs, all lie above the relation between star formation and stellar mass commonly referred to as the Star-Forming Main Sequence (SFMS; Figs. 5 & 6); we confirm this is true even if we include UV only SFRs. The ELGs tend to lie ~ 0.9 dex above the SFMS at $z = 3.5$ as measured by Tomczak et al. (2016) from stacked SFRs based on (UV+IR) fluxes from ZFOURGE. The overall distribution of the spectroscopically confirmed Strong ELGs mirrors that of the photometrically selected sample at this epoch, *i.e.* most of the SELGs lie above the SFMS.

With stellar mass-doubling time-scales of only $\sim 10 - 100$ Myr, virtually all of the Strong ELGs are starbursts (Figs. 5 & 6). Our results are consistent with Amorín et al. (2017) and Maseda et al. (2014) who find that Strong ELGs at $1 < z < 3$ have elevated SFRs for their given stellar mass. At stellar masses of $\log(M_\star/M_\odot) \sim 9 - 9.5$ where the two redshift samples overlap, our SELGs at $2.5 < z_{\rm phot} < 4.0$ have higher SFRs compared to the $z \sim 2$ SELGs. However, we note that for low mass galaxies ($\log(M_\star/M_\odot) \lesssim 10$), the observed scatter in $M_\star$-SFR increases with increasing redshift (Tomczak et al. 2016).

A possible concern is that our (UV+IR) based SFRs are near or below the nominal IR detection limit at $z \sim 3.5$ (Tomczak et al. 2016). However, the very lack of IR emission is consistent with SELGs having little to no dust. We find additional support for the elevated SFRs and specific SFRs for the SELGs in Cohn et al. (2018): using the SED fitting code Prospector (Conroy et al. 2009; Leja et al. 2017), Cohn et al. (2018) show that the Strong ELGs with Hβ+[O III] $EW_{\rm rest} \gtrsim 800$Å ($S_1$ELG) are dominated by the current starburst and have rising star formation rates.

3.4. *Galaxy Size vs. Stellar Mass*

Our Emission Line Galaxies lie on the galaxy size-mass ($r_{\rm eff}$-$M_\star$) relation measured by Allen et al. (2017) using ZFOURGE galaxies at $3 < z_{\rm phot} < 3.75$ (Fig. 7). Here we use the effective radii (galaxy size) measured by van der Wel et al. (2012) with the WFC3/F160W imaging and consider only galaxies with goodness of fit flag of 0. These criteria further reduce our ELG sample to 13 galaxies. We note that relaxing the goodness of fit flag to include all ELGs with measured $r_{\rm eff}$ (28) increases the scatter in the galaxy size-mass relation but does not change the overall result.

Although they are virtually all starbursts (Figs. 5 & 6), our ELGs at $2.5 < z_{\rm phot} < 4.0$ follow the same $r_{\rm eff}$-$M_\star$ relation as the general population. The Strong ELGs at $1 < z < 3$ (Maseda et al. 2014) are also consistent with the same size-mass relation except for the lowest mass systems ($\log(M_\star/M_\odot) < 8.5$) which tend to lie below this relation, i.e. they are more compact at a given stellar mass. Combining both redshift samples suggests that the Strong ELGs are an early phase in the continuum of stellar growth.

3.5. *Inferred Gas Fractions*

With UV+IR luminosities from ZFOURGE and $r_{\rm eff}$ from the HST/F160W imaging (van der Wel et al. 2012), we use the Schmidt-Kennicutt Relation (SKR; Schmidt 1959; Kennicutt 1998, Eq. 7) to estimate the gas surface density for individual galaxies:

$$\Sigma_{\rm SFR} = (2.5 \pm 0.7) \times 10^{-4} \left(\frac{\Sigma_{\rm gas}}{1 M_\odot \ {\rm pc}^{-2}} \right)^{1.4 \pm 0.15} M_\odot \ {\rm year}^{-1} \ {\rm kpc}^{-2} \tag{2}$$

Assuming that half of the gas mass is within $r_{\rm eff}$, we use $\Sigma_{\rm SFR}$ to estimate the total gas mass:

$$\log(M_{\rm gas}) = \frac{5}{7} \log(L_{\rm UV+IR}) + \frac{2}{7} \log[\pi (r_{\rm eff})^2] + 1.52 \tag{3}$$

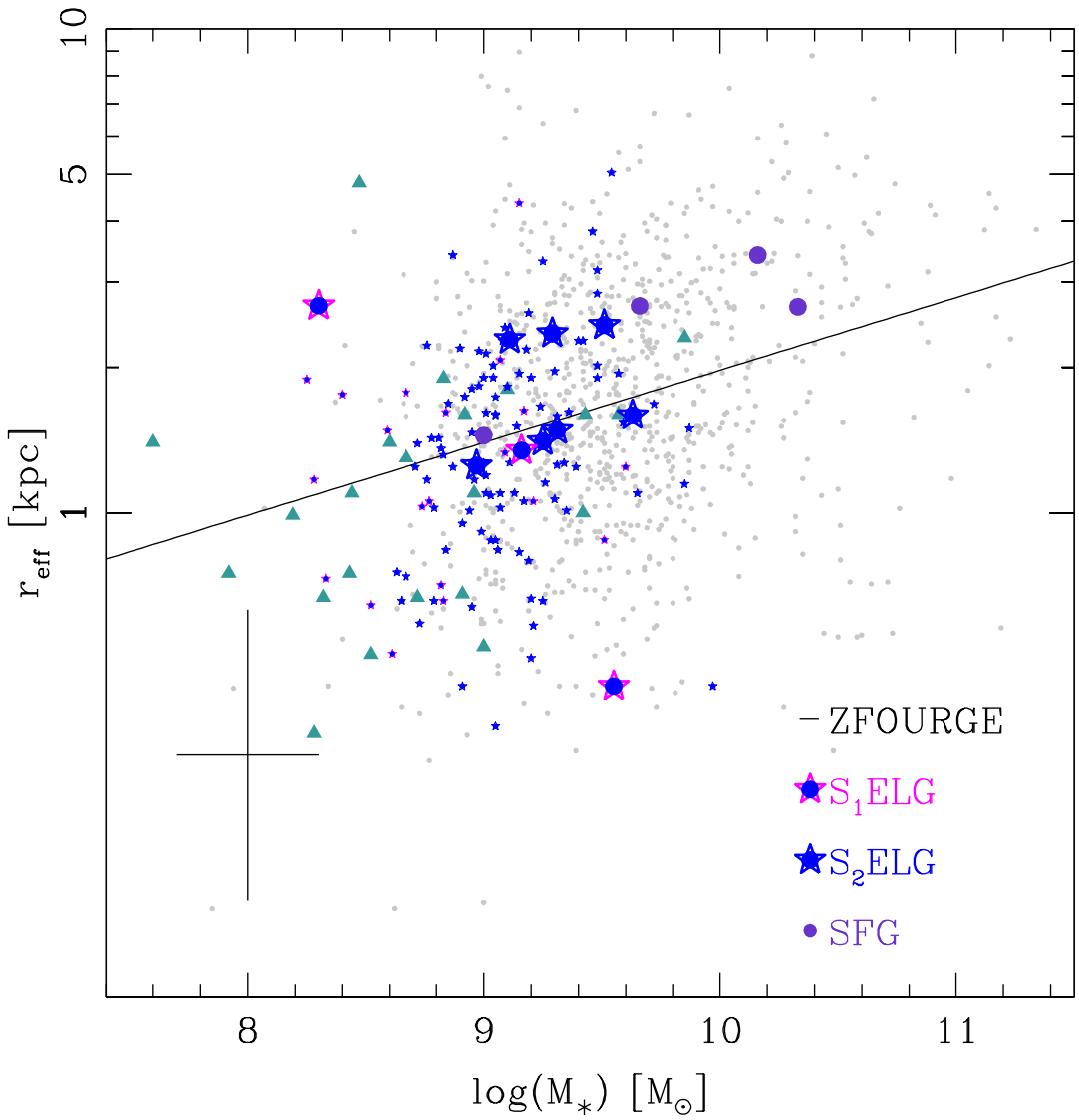

Figure 7. The Hβ+[O III] emitters are consistent with the ZFOURGE galaxy size-stellar mass relation at 3 $<z_{\rm phot}<$ 3.75 from Allen et al. (2017) (solid line), but there is considerable scatter both in the ELGs and for all ZFOURGE galaxies at 2.5 $<z_{\rm phot}<$ 4.0. Here we use the effective radii measured by van der Wel et al. (2012) with WFC3/F160W imaging and the symbols are as in Fig. 5. The illustrative errorbars correspond to a factor of two uncertainty in stellar mass and galaxy size. The strong ELGs at $z \sim 2$ (filled triangles; Maseda et al. 2014) are consistent with the same mass-size relation except at the lowest mass ($\log(M_\star/M_\odot)<$ 8.5) where they tend to be more compact.

where $r_{\rm eff}$ is measured in kpc, $M_{\rm gas}$ in $M_\odot$, and $L_{\rm UV+IR}$ in $L_\odot$; see also Papovich et al. (2015). We use $r_{\rm eff}$ defined by the stellar light; note that studies using CO (Tacconi et al. 2013) and Hα (Förster Schreiber et al. 2011) find $r_{\rm eff}$ from gas and stars are consistent. Assuming an observational detection limit of $L_{\rm UV+IR}= 10^{11}$ $L_\odot$ and typical galaxy size of $r_{\rm eff}= 3.2$ kpc (Tran et al. 2017), the corresponding gas mass limit is $\log(M_{\rm gas}/M_\odot)= 9.8$. Gas fractions are defined to be $M_{\rm gas}/(M_{\rm gas}+M_\star)$.

All of our spectroscopically confirmed ELGS have inferred gas fractions of $f_{\rm gas}> 60\%$ (Fig. 8) which is not surprising given the ELGs' high specific star formation rates and our detection limits. The

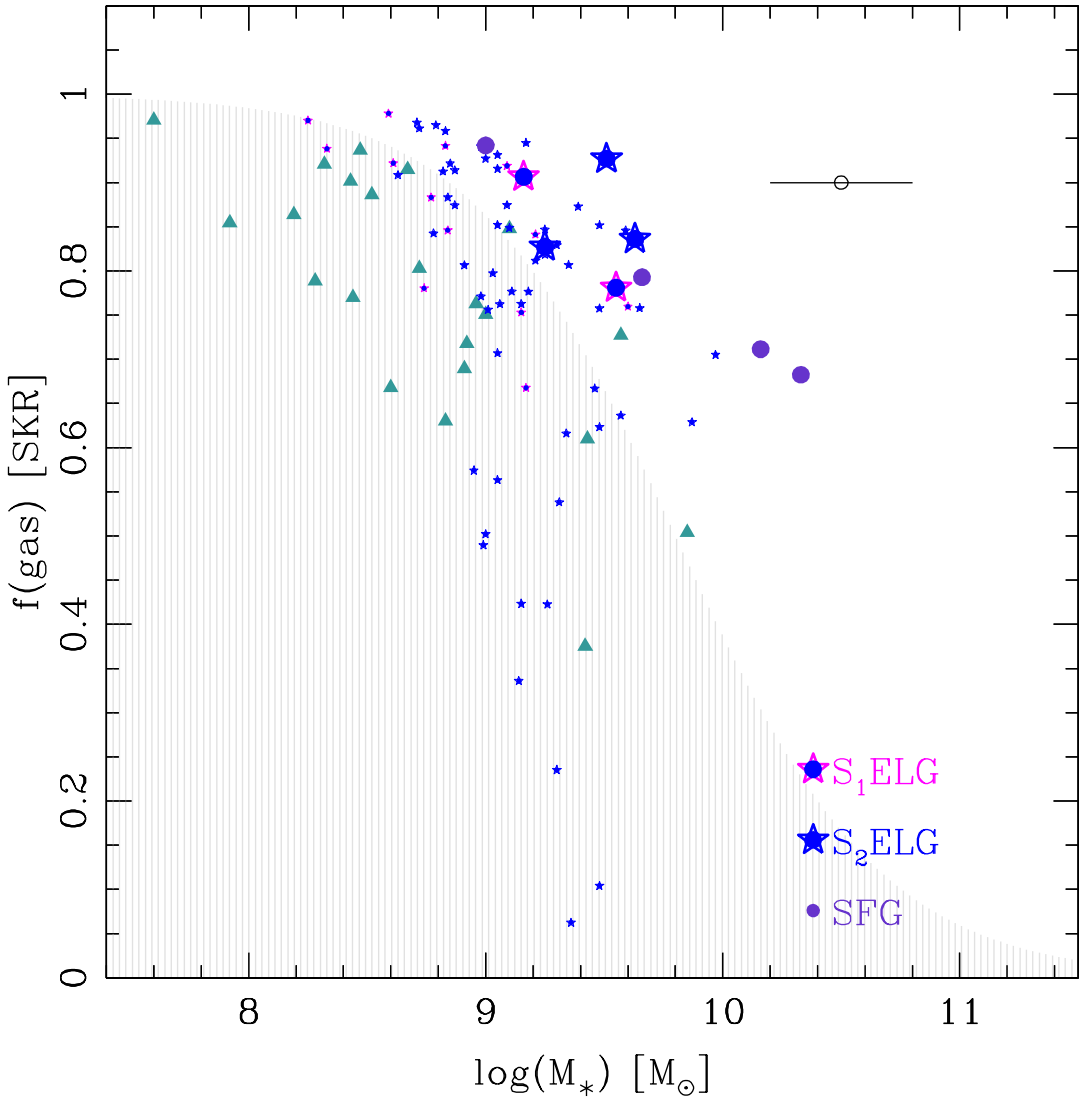

Figure 8. We infer gas masses by using the Schmidt-Kennicutt Relation (SKR; Kennicutt 1998) with effective sizes from vdW12 and total luminosities from Tomczak et al. (2016); symbols are as in Figs. 4 & 5. The illustrative errorbars correspond to a factor of two uncertainty in stellar mass and we note that the gas mass is highly uncertain. For reference, we show the exclusion region corresponding to a gas mass limit of $\log(M_\star/M_\odot)= 9.8$ (light gray shaded region) which is below our nominal detection threshold at $z \gtrsim 3$. All of the spectroscopically confirmed ELGs in our study have inferred gas mass fractions of $f_{gas}> 60\%$, but this is expected given the combination of their high specific star formation rates (see Fig. 6) and our detection limits at $z \sim 3.5$. The SELGs will move to the right as they increase in stellar mass and, unless their gas reservoirs are replenished, downwards.

high gas masses are consistent with high accretion rates that may be driving the star formation (Kacprzak et al. 2016). Our inferred gas fractions combined with measurements of Strong ELGs at $z \sim 2$ (Maseda et al. 2014) suggests that $f_{gas}\gtrsim 80\%$ for ELGs with stellar masses of $\log(M_\star/M_\odot)< 9$. However, direct measurements of gas masses for the ELGs at $z > 2$ with stellar masses of $\log(M_\star/M_\odot)< 9$ will be difficult given current observational limitations.

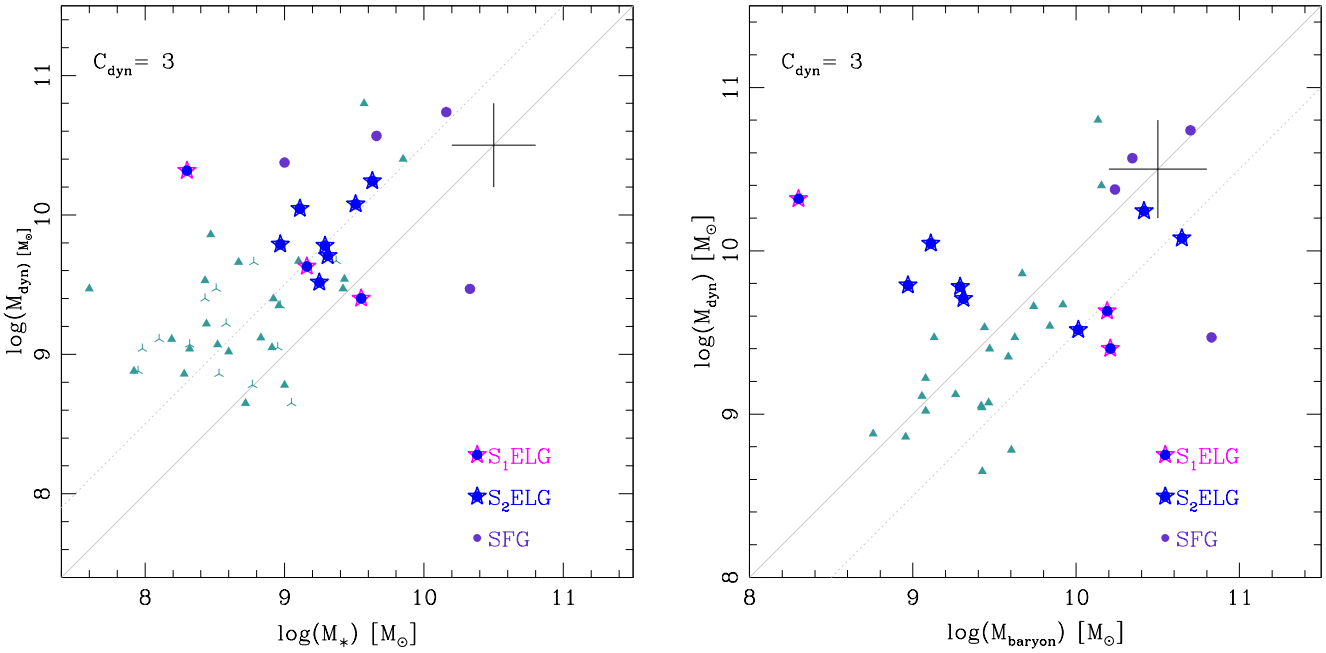

Figure 9. *Left:* The dynamical masses for the [O III]5007Å emitting galaxies at $3 < z_{\rm spec} < 3.8$ are ~ 0.4 dex larger than their stellar masses (symbols are as in Fig. 3). The illustrative errorbars correspond to a factor of two uncertainty in mass. We estimate virial masses by combining the [O III]5007Å line-widths with effective radii measured by vdW12 (see Alcorn et al. 2016, 2018). The solid diagonal line is parity and the dotted line is offset by 0.5 dex. Our results are consistent with studies showing that ELGs at $z \sim 2$ tend to have $M_{\rm dyn}>M_\star$(Maseda et al. 2013; Maseda et al. 2014) and with their inferred gas mass fractions of $f_{\rm gas}> 60\%$. *Right:* The same `MOSEL` galaxies where we now compare the total baryonic mass (sum of the stellar and estimated gas mass) to their dynamical mass. Including $f_{\rm gas}$ brings the `MOSEL` galaxies closer to parity, but we hesitate to draw any stronger conclusions given the scatter and low number statistics.

3.6. *Kinematics*

The integrated velocity dispersions ($\sigma_{\rm int}$) based on [O III]5007Å line-widths is $\sigma_{\rm int}\sim 40-150$ km s^{-1} for most of the ELGs with only one ELG having $\sigma_{\rm int}\sim 200$ km s^{-1} (see Tables 1 & 2). Combining $\sigma_{\rm int}$ and effective radii from vdW12, we follow Alcorn et al. (2016) and estimate virial masses:

$$M_{\rm dyn}(< R_e) = K_e \frac{\sigma_{\rm int}^2 R_e}{G} \tag{4}$$

where for consistency with Maseda et al. (2013); Maseda et al. (2014), we adopt the virial factor $K_e = 3$ which is typically used for disk galaxies.

The dynamical masses for our ELGs at $3 < z_{\rm spec} < 3.8$ are ~ 0.4 dex larger than their stellar masses (Fig. 9); the handful of galaxies with $M_{\rm dyn}<M_\star$ is consistent with scatter due to errors in the measurements. The offset between virial and stellar mass is consistent with measurements of Strong ELGs at $z \sim 2$ (Maseda et al. 2013; Maseda et al. 2014) and continues the same trend to higher masses. Within our limited sample at $3 < z_{\rm spec} < 3.8$, there is no obvious difference in the $M_\star$-$M_{\rm dyn}$ relation for Strong ELGs compared to higher mass ($\log(M_\star/M_\odot)> 9$) star-forming galaxies.

When comparing the total baryonic mass (sum of the stellar and estimated gas mass) to dynamical mass, we find that the MOSEL galaxies are closer to parity (Fig. 9, left). However, given the scatter and low number statistics, we hesitate to draw any stronger conclusions regarding the ratio of dark to baryonic mass for the MOSEL galaxies.

3.7. *Star Formation or Active Galactic Nuclei?*

Our analysis assumes that the strong [O III]5007Å emission is driven by star formation and not Active Galactic Nuclei (AGN). We have used the ZFOURGE catalog by Cowley et al. (2016) to remove AGN but recognize that at $z > 3$, the multi-wavelength AGN diagnostics may not be reliable especially given the uneven coverage across these fields. However, the [O III]5007Å line-widths are consistent with star formation: most of the ELGs have $\sigma_{\rm int} \sim 40 - 150$ km s^{-1} with only one ELG having $\sigma_{\rm int} \sim 200$ km s^{-1} (see Tables 1 & 2). Also, our recent results using Prospector to construct the star formation histories of the strong ELGs confirms that they are dominated by starbursts spanning the most recent ~ 50 Myr (Cohn et al. 2018). Lastly, we note that AGN contamination is rare in low-mass galaxies (e.g., Ho et al. 1997; Trump et al. 2015).

Unlike the ZFOURGE composite SEDs where Hβ and [O III]5007Å are blended (Forrest et al. 2017), the MOSFIRE spectroscopy easily resolves these spectral features for individual ELGs. Thus we also can identify potential AGN by combining the ratio of [O III]5007Å to Hβ with stellar mass (Juneau et al. 2011), although we note this method is contested at $z > 1$ (Trump et al. 2013). The median [O III]5007/Hβ value for our sample of ELGs is ~ 5.8 which is consistent with values reported by (Holden et al. 2016) for Lyman-Break Galaxies at $z \sim 3$. Following a similar line of analysis, Maseda et al. (2014) also excluded AGN from their sample of strong ELGs at $1 < z < 2$.

Hβ is weaker than [O III]5007Å and given our line-flux limit of $\sim 3 \times 10^{-18}$erg s^{-1} cm^{-2} (3σ), we can only place upper limits on the ratio of [O III]5007/Hβ for many of the ELGs. A more careful treatment of the Hβ line-fluxes, e.g. by stacking the spectra, can be used to constrain ISM conditions. Further analysis that includes Hβ, e.g. by combining [O III]5007/Hβ with stellar masses and star formation histories, will be presented in a future MOSEL paper.

4. DISCUSSION

With deep multi-band photometry from ZFOURGE, we identified Emission Line Galaxies at $z > 2.5$ that have blended rest-frame Hβ+[O III] equivalent widths of $\gtrsim 230$Å (Forrest et al. 2017, 2018). We consider the combined sample of Strong ELGs grouped in the two composite SEDs with the largest Hβ+[O III] equivalent widths (EW$_{\rm rest}$> 230Å; see §2.1.2). The rarity of ELGs with EW$_{\rm rest}$([O III]5007)$\gtrsim$ 200Å in the local Universe (~ 2 "green peas" per square degree; Cardamone et al. 2009) raises the question of whether this Strong emission line phase is the exception or the norm at high redshifts. In our MOSEL survey, we build on recent studies to further explore how galaxies at $z \sim 3.5$ with strong [O III]5007Å emission fit into our current understanding of how star-forming galaxies grow by combining Keck/MOSFIRE K-band spectroscopy with our existing multi-band photometry from ZFOURGE.

4.1. *Strong [O III]5007Å Emission May Be Common in Early Galaxy Formation*

We spectroscopically confirm 31 galaxies at $3 < z_{\rm spec} < 3.8$ with stellar masses of $\log(M_\star/M_\odot) \sim 8.2 - 10.2$ and rest-frame [O III]5007Å equivalent widths up to ~ 500Å (Figs. 1 & 3). The properties of the spectroscopically confirmed Strong ELGs mirror that of the larger photometrically selected

sample (e.g. Figs. 4 & 5). Most of the SELGs have blue colors of $(V-J)< 0$ while the more typical star-forming galaxies have $(V-J)\sim 0-1$ (Fig. 4). The overlapping ranges in their rest-frame UVJ colors suggest that the Strong ELGs transition into more massive star-forming galaxies, e.g. Lyman-Break Galaxies.

In the stellar mass range where we overlap with MOSDEF galaxies at $z\sim 2$ (Reddy et al. 2018), we find a similar relationship between [O III]5007Å $\mathrm{EW_{rest}}$ and stellar mass (Fig. 3). Reddy et al. (2018) suggest that the increasing [O III]5007Å $\mathrm{EW_{rest}}$ with decreasing stellar mass can be explained by either rapid enrichment of α elements or metallicities of $\lesssim 0.2Z_\odot$ for galaxies with $\log(\mathrm{M_\star/M_\odot})\lesssim 9$. Both scenarios are consistent with our interpretation that the SELGs are young and have sub-solar metallicities.

In combination with Cohn et al. (2018) who show that SELGs at $z\sim 3.5$ have low gas-phase metallicites ($Z_\star\lesssim 0.02Z_\odot$) and higher specific star formation rates relative to SFGs (4.6 Gyr$^-$1 vs 1.1 Gyr$^-$1), our spectroscopic measurements support a scenario where strong [O III]5007Å emission signals the earliest episodes of intense star formation (see also Amorín et al. 2017). As the SELGs grow in stellar mass, the growing amount of continuum light means that even during subsequent episodes of bursty star formation, the [O III]5007Å equivalent widths will not be as large as during the first major burst of star formation. With star formation rates of $\gtrsim 3-250$ $\mathrm{M_\odot\ yr^{-1}}$ (Fig. 5) and mass-doubling times of $\sim 10-100$ Myr (Figs. 5 & 6), the intense [O III]5007Å emission phase is brief as these same galaxies quickly transition into more typical star-forming galaxies with Hβ+[O III] $\mathrm{EW_{rest}}\lesssim 230$Å.

We find further support for a picture where strong [O III]5007Å emission signals the earliest stages of stellar growth in galaxies by comparing relations between stellar mass ($\mathrm{M_\star}$), galaxy size ($\mathrm{r_{eff}}$), and virial mass ($\mathrm{M_{dyn}}$). Our SELGs follow the same general $\mathrm{M_\star}$-$\mathrm{r_{eff}}$ relation as that of star-forming galaxies at $z\sim 3$ (Fig. 7), although we note the large scatter for all galaxies at this epoch. The SELGs also continue the same trend between $\mathrm{M_{dyn}}$-$\mathrm{M_\star}$ as measured for SELGs at $z\sim 2$ (Fig. 9). The SELGs have virial masses that are larger by ~ 0.4 dex relative to their stellar masses which is consistent with their inferred gas mass fractions of $\mathrm{f_{gas}}> 60\%$ (Fig. 8).

In a recent paper (Cohn et al. 2018), we derived galaxy properties from the `ZFOURGE` photometry using the SED-fitting code `Prospector` (Leja et al. 2017) and the Flexible Stellar Population Synthesis package (FSPS; Conroy et al. 2009). The `Prospector` code finds the best fit model and estimates uncertainties by sampling the posterior probability distributions of all the free parameters. By calculating nonparametric star formation histories, `Prospector` can distinguish between rising, falling, and bursty star formation histories.

Using `Prospector`, Cohn et al. (2018) show that ELGs with extreme emission ($\mathrm{S_1}$ELG; Hβ+[O III] $\mathrm{EW_{rest}}\gtrsim 800$Å) are "first burst" systems and likely to have rising star formation rates. These same galaxies have low gas-phase metallicities of $Z_*\lesssim 0.02Z_\odot$ and higher specific star formation rates compared to star-forming galaxies: ~ 4.6 Gyr^{-1} vs. ~ 1.1 Gyr^{-1}. Cohn et al. (2018) inferred that many, if not most, star-forming galaxies at $z>2.5$ have Extreme Hβ+[O III] emission-line phases early in their formation histories. As these "first burst" systems continue to form stars and chemically enrich to evolve into more typical SFGs, they move diagonally from the upper left to the bottom right in Figs. 6 & 8.

4.2. *A Potential Source of Ionizing UV Photons*

A growing number of studies indicate that galaxies rather than AGN generated the UV photons needed to ionize the universe, but there are not enough massive galaxies at $z \gtrsim 6$ to generate the required UV photons (Robertson et al. 2013; Robertson et al. 2015). With several low-mass ($\log(M_\star/M_\odot) \lesssim 9$) systems now identified at $z > 3$ that have strong EW_{rest}([O III]5007)> 300Å and escape fractions of $f_{esc} \gtrsim 10\%$ (Nakajima et al. 2016; de Barros et al. 2016), the most viable source of UV photons are these low-mass, star-bursting galaxies. However, the stellar mass function at $z > 8$ must be steeper than observed at lower redshifts for there to be enough of these dwarf galaxies to generate the required UV photons.

Another potential source of UV photons are the galaxies in our study with EW_{rest}([O III]5007)$>$ 200Å, e.g galaxies in a strong emission line phase. The inferred gas fractions of $f_{gas} \gtrsim 60\%$ (Fig. 8) and high specific star formation rates (Fig. 6) imply that the ELGs with the strongest [O III]5007Å easily increase their stellar masses by factors > 2 in less than ~ 100 Myr, i.e. these Strong ELGs signal the earliest stages of stellar growth in galaxies (see also Cohn et al. 2018).

If the [O III]5007Å emitters also have large [O III]5007/[O II]3727 ratios (O32$\gtrsim 5$), studies indicate they may leak more Lyman-Continuum photons due to their harder ionizing spectrum (Izotov et al. 2016; Nakajima & Ouchi 2014; Nakajima et al. 2016). Tang et al. (2019) find that in the most intense line emitters at $z \sim 2$, the ionizing photon efficiency scales with [O III]5007Å emission. However, recent results by Bassett et al. (2019) of galaxies at $z \sim 3$ suggest that the correlation between large [O III]5007/[O II]3727 ratios and more Ly-C photons is weak at best, and Naidu et al. (2018) constrain the average escape fractions for SELGs to be $8.5 - 16.7\%$.

Only with spectroscopy can we measure fluxes of oxygen lines for individual galaxies to measure their ratios and determine what drives the strong [O III]5007 emission, e.g. shocks or massive binary stars (Strom et al. 2017). By obtaining at $z \sim 3.5$ the ratio of [O III]5007 to well-studied emission lines such as [O II]3727, Hβ, and Lyα (e.g. Tang et al. 2019; Bassett et al. 2019), we can better track how the ionizing photon efficiency evolves from the first galaxies to $z \sim 0$. We plan to measure [O II]3727Å emission for our ELGs to characterize their ionization conditions and constrain their production of Lyman-Continuum photons.

5. CONCLUSIONS

Our Multi-Object Spectroscopic Emission Line (`MOSEL`) survey focuses on galaxies with strong [O III]5007Å emission identified using deep broad-band photometry from the `ZFOURGE` survey (Forrest et al. 2017, 2018). We use Keck/MOSFIRE K-band spectroscopy and measure redshifts of 49 galaxies at $2.091 < z_{spec} < 4.751$. Our spectroscopic success rate is $\sim 53\%$ and z_{phot} uncertainty is $\sigma_z = [\Delta z/(1+z)] = 0.0135$ (§2.2.2, Fig. 1; see also Straatman et al. 2016; Nanayakkara et al. 2016).

Of the 49 spectroscopically confirmed galaxies at $2.091 < z_{spec} < 4.751$, we measure [O III]5007Å line fluxes for 31 galaxies at $3 < z_{spec} < 3.8$ (Fig. 2). By dividing the line-flux as measured with MOSFIRE by the continuum flux from `ZFOURGE`, we estimate rest-frame [O III]5007Å equivalent widths of $\sim 100 - 500$Å where EW_{rest} increases with decreasing stellar mass (Fig. 3). Our analysis focuses on the Strong Emission Line Galaxies (SELGs) grouped in the two composite SEDs with the strongest Hβ+[O III] emission ($EW_{rest} > 230$Å) from Forrest et al. (2018).

We explore the properties of SELGs at $z \sim 3.5$ to connect them to our current picture of star-forming galaxies. The physical properties of the spectroscopically confirmed [O III]5007Å Strong Emission Line Galaxies (SELGs) mirror that of the larger photometrically selected sample. For

example, the SELGs tend to have bluer colors of $(V-J)< 0$ compared to more typical star-forming galaxies with $(V-J)\sim 0-1$ (Fig. 4).

The Strong Hβ+[O III] emitting galaxies in our study have stellar masses of $\log(M_\star/M_\odot)\sim 8.2-9.6$ (Fig. 5). The same galaxies lie ~ 0.9 dex above the star-forming main sequence at $z = 3.5$ and have high specific star-formation rates with mass-doubling timescales of $\sim 10-100$ Myr (Fig. 6). The inferred gas fractions of $f_{gas}\gtrsim 60\%$ (Fig. 8) can easily fuel a burst that increases stellar mass by > 2. In terms of stellar and virial mass, (UV+IR) star formation rate, and galaxy size, our Hβ+[O III] emitting galaxies bridge relations measured for Strong ELGs at $1 < z < 3$ ($\log(M_\star/M_\odot)\lesssim 9$; van der Wel et al. 2011; Maseda et al. 2014) to star-forming galaxies at $z \sim 3.5$ (see Figs. 5, 6, & 7).

Taken as a whole, our analysis suggests that strong [O III]5007Å emission ($EW_{rest}\gtrsim 200$) signals an early episode of intense star formation in low-mass ($M_\star < 0.1\ M^\star$) galaxies at $z \gtrsim 3$. The ELGs with the strongest [O III]5007Å are a rapidly evolving population of galaxies both in number density and stellar growth (Forrest et al. 2017; Cohn et al. 2018). The [O III]5007Å ELGs are likely to evolve into more massive and older star-forming galaxies with stable disks and bulges, e.g. Lyman-Break Galaxies.

In a recent paper (Cohn et al. 2018), we estimated that many, if not most, star-forming galaxies at $z > 3$ are strong [O III]5007Å emitters early in their formation history. If strong [O III]5007Å emission is a common phase in early galaxy formation, this brief episode may generate a significant number of ionizing UV photons. In a future paper, we will explore additional line diagnostics, e.g. the ratio of [O III]5007Å to Hβ, to characterize ionization conditions and constrain the production of Lyman-Continuum photons in galaxies with the strongest [O III]5007Å emission.

ACKNOWLEDGMENTS

We are grateful to the Keck/MOSFIRE team with special thanks to M. Kassis, J. Lyke, G. Wirth, and L. Rizzi on the Keck support staff. K. Tran thanks P. Oesch, B. Holden, and M. Maseda for helpful discussions, and B. Forrest thanks the Hagler Institute for Advanced Study at Texas A&M for support. We also thank the referee for a thoughtful and constructive report. This work was supported by a NASA Keck PI Data Award administered by the NASA Exoplanet Science Institute. Data presented herein were obtained at the W. M. Keck Observatory from telescope time allocated to NASA through the agency's scientific partnership with the California Institute of Technology and the University of California. The Observatory was made possible by the generous financial support of the W. M. Keck Foundation. K. Tran acknowledges that this material is based upon work supported by the National Science Foundation under Grant Number 1410728 and acknowledges the ARC Centre for Excellence in All-Sky Astrophysics in 3D (ASTRO 3D) for support in preparing the manuscript. GGK acknowledges the support of the Australian Research Council through the DP170103470. The authors wish to recognize and acknowledge the very significant cultural role and reverence that the summit of Mauna Kea has always had within the indigenous Hawaiian community. We are most fortunate to have the opportunity to conduct observations from this mountain.

Table 1. MOSEL Galaxy Properties[a]

Field	ZFOURGE[b] ID	RA[b] J2000	Dec[b] J2000	$z_{\rm spec}$ ±0.003	$z_{\rm phot}$[b] ±0.0135	$K_{\rm obs}$[b] mag	$(U-V)$[b] mag	$(V-J)$[b] mag	$\log(M_\star/M_\odot)$[c]	log(SFR)[c] $M_\odot$ yr^{-1}	$r_{\rm eff}$[d] kpc
COSMOS	1877	150.170425	2.199359	3.1230	3.16	22.92	0.58	0.46	10.2	2.1	3.4
COSMOS	4214	150.177109	2.221284	3.4578	3.38	23.39	1.01	0.89	10.3	2.4	2.7
COSMOS	7239	150.202240	2.254340	3.1198	3.18	23.85	0.24	-1.08	9.0	< 1	0.7
COSMOS	9884	150.072495	2.282637	3.2982	3.39	23.42	0.93	-0.15	9.1	1.4	1.4
COSMOS	11063	150.146133	2.297038	3.0393	3.04	23.63	0.34	-0.22	8.9	< 1	1.8
COSMOS	11284	150.136337	2.298915	3.3016	3.47	23.09	0.32	-0.16	9.4	1.7	2.4
COSMOS	11544	150.147446	2.301592	3.3038	3.36	22.86	0.29	-0.20	9.5	2.3	2.4
COSMOS	12000	150.070665	2.305136	3.2578	3.28	22.88	0.65	0.81	10.2	2.6	···
COSMOS	12105	150.138840	2.306907	3.2976	3.41	23.25	0.54	-0.09	9.2	1.9	1.3
COSMOS	12273	150.147030	2.309289	3.1809	3.29	23.39	0.31	0.03	9.8	2.4	···
COSMOS	12776	150.121275	2.315327	3.4993	3.55	23.69	0.57	1.08	9.8	2.3	···
COSMOS	12922	150.069214	2.315987	3.2556	3.35	23.24	0.47	0.16	9.7	1.8	2.7
COSMOS	14984	150.060333	2.338560	3.3777	3.50	23.29	0.18	-0.38	9.3	< 1	1.5
COSMOS	15625	150.139206	2.345322	3.1841	3.22	23.50	0.36	-0.20	9.2	1.6	1.4
COSMOS	15636	150.065445	2.345667	3.4188	3.51	24.21	0.13	0.29	9.0	2.0	1.4
COSMOS	16067	150.200134	2.349396	3.1885	3.21	22.89	0.47	-0.30	9.2	< 1	1.4
COSMOS	16325	150.203055	2.352349	3.4538	3.55	23.40	0.49	0.22	9.7	2.2	···
COSMOS	16513	150.066735	2.353337	3.4188	3.49	22.89	0.22	-0.35	9.2	< 1	···
COSMOS	16518	150.211500	2.354372	3.3653	3.14	23.47	0.41	0.36	9.9	2.7	···
COSMOS	16984	150.083664	2.358806	3.3273	3.44	23.11	0.38	0.08	9.3	< 1	2.3
COSMOS	17008	150.168793	2.358994	3.4608	3.55	23.76	0.21	0.21	9.0	< 1	1.3
COSMOS	17423	150.115402	2.363473	3.5259	3.55	23.95	0.51	-0.24	9.6	2.2	0.4
COSMOS	17909	150.094330	2.370171	3.1977	3.49	22.58	0.39	-0.15	9.6	2.1	1.6
COSMOS	18022	150.079529	2.367794	3.4188	3.48	23.89	0.15	-0.28	9.1	< 1	2.3
COSMOS	20001	150.214305	2.378608	3.4488	3.54	22.93	0.39	-0.22	9.4	2.4	···
CDFS	22136	53.152866	-27.749243	3.0883	3.19	22.93	0.34	-0.52	9.2	0.8	1.6
CDFS	15782	53.174133	-27.800318	3.0651	3.15	24.30	0.61	0.08	9.0	2.1	0.2
CDFS	18053	53.195736	-27.782713	3.3239	3.31	24.73	0.21	-0.38	8.6	1.2	0.4
CDFS	17189	53.198280	-27.789150	3.5506	3.54	24.73	0.39	-0.59	8.3	< 1	2.7
CDFS	14864	53.204610	-27.806757	3.5552	3.47	22.52	0.06	-0.16	9.7	1.6	···
CDFS	15561	53.219540	-27.802586	3.0865	3.03	24.68	0.67	-0.41	8.9	< 1	0.4

[a] We include only MOSEL galaxies with spectroscopic redshift quality flag of $Q_z \geq 2.5$ (see Tran et al. 2015; Nanayakkara et al. 2016).

[b] Galaxy identification numbers, observed ZFOURGE K-band magnitudes, photometric redshifts, and rest-frame UVJ are from ZFOURGE (Straatman et al. 2016). Uncertainties on the magnitudes and colors are < 0.01.

[c] We use the stellar masses from Forrest et al. (2018) and the combined UV+IR star formation rates from Tomczak et al. (2016). We recommend the reader consider a typical uncertainty of ~ 0.3 dex for both parameters.

[d] Effective radii are from van der Wel et al. (2012) and measured using the WFC3/F160W imaging. Here we take the sizes reported in arcsec and convert to kpc using the angular diameter distance.

Table 2. MOSEL: [O III]5007Å Properties

Field	ZFOURGE[a]	f(5007Å)[b]	σ_{1D}[b]	σ_{int}[b]	EW_{rest}[c]
	ID	10^{-17} erg s^{-1} cm^{-2}	Å	km s^{-1}	Å
COSMOS	1877	2.2 ±0.6	10.5	151	23.3
COSMOS	4214	1.4 ±1.1	3.0	39	23.0
COSMOS	7239	10.1 ±0.3	4.3	62	542
COSMOS	9884	10.5 ±0.6	9.0	124	392
COSMOS	11063	17.3 ±0.4	4.1	60	468
COSMOS	11284	16.8 ±0.9	4.9	68	262
COSMOS	11544	12.3 ±0.6	6.0	83	153
COSMOS	12000	8.3 ±0.4	8.5	119	78.0
COSMOS	12105	9.6 ±0.7	4.9	67	221
COSMOS	12273	8.0 ±0.5	7.7	110	78.6
COSMOS	12776	11.5 ±1.6	8.7	116	199
COSMOS	12922	4.9 ±1.1	10.0	141	67.6
COSMOS	14984	8.1 ±0.2	5.1	70	228
COSMOS	15625	8.7 ±0.3	4.1	58	199
COSMOS	15636	4.8 ±0.5	11.4	154	514
COSMOS	16067	24.8 ±0.4	6.3	90	428
COSMOS	16325	6.7 ±1.3	7.8	105	109
COSMOS	16513	13.0 ±0.6	4.3	58	289
COSMOS	16518	4.3 ±1.0	8.3	113	40.8
COSMOS	16984	14.7 ±0.3	4.4	60	405
COSMOS	17008	10.6 ±0.8	6.3	84	399
COSMOS	17423	12.3 ±1.1	6.9	90	285
COSMOS	17909	22.5 ±0.7	8.8	125	248
COSMOS	18022	6.5 ±0.4	6.2	83	282
COSMOS	20001	22.0 ±0.5	7.3	97	378
CDFS	22136	2.8 ±0.7	14.3	208	97.0
CDFS	15782	2.6 ±0.5	6.6	96	240
CDFS	18053	1.0 ±0.6	3.6	49	165
CDFS	17189	2.3 ±0.4	8.0	105	506
CDFS	14864	2.7 ±0.3	10.8	142	46.6
CDFS	15561	3.2 ±0.2	2.8	41	430

[a] Galaxy identification numbers are from ZFOURGE (Straatman et al. 2016).

[b] [O III]5007Å line-flux, line-width (σ_{1D}), and the corresponding integrated velocity dispersion (σ_{int}) are measured by fitting a Gaussian to the MOSFIRE spectra (see §2.2.3).

[c] [O III]5007Å rest-frame equivalent widths are determined using the line flux measured with MOSFIRE spectroscopy and continuum flux from the best-fit FAST SED (see §2.2.4).

REFERENCES

Alcorn, L. Y., Tran, K.-V. H., Kacprzak, G. G., et al. 2016, ApJL, 825, L2

Alcorn, L. Y., Tran, K.-V., Glazebrook, K., et al. 2018, ApJ, 858, 47

Allen, R. J., Kacprzak, G. G., Glazebrook, K., et al. 2017, ApJL, 834, L11

Amorín, R., Fontana, A., Pérez-Montero, E., et al. 2017, Nature Astronomy, 1, 0052

Amorín, R., Pérez-Montero, E., Contini, T., et al. 2015, A&A, 578, A105

Amorín, R., Pérez-Montero, E., Vílchez, J. M., & Papaderos, P. 2012, ApJ, 749, 185

Atek, H., Siana, B., Scarlata, C., et al. 2011, The Astrophysical Journal, 743, 121

Bassett, R., Ryan-Weber, E. V., Cooke, J., et al. 2019, MNRAS, 483, 5223

Bian, F., Kewley, L. J., Dopita, M. A., & Juneau, S. 2016, ApJ, 822, 62

Bruzual, G., & Charlot, S. 2003, MNRAS, 344, 1000

Cardamone, C., Schawinski, K., Sarzi, M., et al. 2009, Monthly Notices of the Royal Astronomical Society, 399, 1191

Ceverino, D., Klessen, R., & Glover, S. 2018, ArXiv e-prints, arXiv:1801.10382

Cohn, J. H., Leja, J., Tran, K.-V. H., et al. 2018, ApJ, 869, 141

Conroy, C., Gunn, J. E., & White, M. 2009, ApJ, 699, 486

Cowley, M. J., Spitler, L. R., Tran, K.-V. H., et al. 2016, MNRAS, 457, 629

de Barros, S., Vanzella, E., Amorín, R., et al. 2016, A&A, 585, A51

Elbaz, D., Dickinson, M., Hwang, H. S., et al. 2011, A&A, 533, A119

Ferland, G. J., Porter, R. L., van Hoof, P. A. M. andWilliams, R. J. R., et al. 2013, RMxAA, 49, 137

Forrest, B., Tran, K.-V. H., Broussard, A., Allen, R. J., & et al. 2017, ApJL, 838, L12

Forrest, B., Tran, K.-V. H., Broussard, A., et al. 2018, ApJ, 863, 131

Forrest, B., Tran, K.-V. H., Tomczak, A. R., et al. 2016, ApJL, 818, L26

Förster Schreiber, N. M., Shapley, A. E., Erb, D. K., et al. 2011, ApJ, 731, 65

Giacconi, R., Zirm, A., Wang, J., et al. 2002, The Astrophysical Journal Supplement Series, 139, 369

Grogin, N. A., Kocevski, D. D., Faber, S. M., et al. 2011, ApJS, 197, 35

Guo, Y., Rafelski, M., Faber, S. M., et al. 2016, ApJ, 833, 37

Ho, L. C., Filippenko, A. V., & Sargent, W. L. W. 1997, ApJ, 487, 568

Holden, B. P., Oesch, P. A., González, V. G., et al. 2016, The Astrophysical Journal, 820, 73

Izotov, Y. I., Guseva, N. G., Fricke, K. J., & Henkel, C. 2016, MNRAS, 462, 4427

Izotov, Y. I., Guseva, N. G., & Thuan, T. X. 2011, The Astrophysical Journal, 728, 161

Izotov, Y. I., Schaerer, D., Worseck, G., et al. 2018, MNRAS, 474, 4514

Jaskot, A. E., & Oey, M. S. 2013, ApJ, 766, 91

Juneau, S., Dickinson, M., Alexander, D. M., & Salim, S. 2011, ApJ, 736, 104

Kacprzak, G. G., van de Voort, F., Glazebrook, K., et al. 2016, ApJL, 826, L11

Kennicutt, R. C. 1998, ARA&A, 36, 189

Koekemoer, A. M., Faber, S. M., Ferguson, H. C., et al. 2011, ApJS, 197, 36

Kriek, M., van Dokkum, P. G., Labbé, I., et al. 2009, ApJ, 700, 221

Kriek, M., van Dokkum, P. G., Whitaker, K. E., et al. 2011, ApJ, 743, 168

Krumholz, M. R., Burkhart, B., Forbes, J. C., & Crocker, R. M. 2017, ArXiv e-prints, arXiv:1706.00106

Lawrence, A., Warren, S. J., Almaini, O., et al. 2007, MNRAS, 379, 1599

Leja, J., Johnson, B. D., Conroy, C., van Dokkum, P. G., & Byler, N. 2017, ApJ, 837, 170

Lofthouse, E. K., Houghton, R. C. W., & Kaviraj, S. 2017, MNRAS, 471, 2311

Maseda, M. V., van der Wel, A., da Cunha, E., et al. 2013, The Astrophysical Journal, 778, L22

Maseda, M. V., van der Wel, A., Rix, H.-W., Momcheva, I., & et al. 2018, ApJ, 854, 29

Maseda, M. V., van der Wel, A., Rix, H.-W., et al. 2014, ApJ, 791, 17

McLean, I. S., Steidel, C. C., Epps, H. W., Konidaris, N., & et al. 2012, in Society of Photo-Optical Instrumentation Engineers (SPIE) Conference Series, Vol. 8446, Society of Photo-Optical Instrumentation Engineers (SPIE) Conference Series
Mitra, S., Ferrara, A., & Choudhury, T. R. 2013, MNRAS, 428, L1
Momcheva, I. G., Brammer, G. B., van Dokkum, P. G., et al. 2016, ApJS, 225, 27
Naidu, R. P., Forrest, B., Oesch, P. A., Tran, K.-V. H., & Holden, B. P. 2018, MNRAS, 478, 791
Nakajima, K., Ellis, R. S., Iwata, I., et al. 2016, ApJL, 831, L9
Nakajima, K., & Ouchi, M. 2014, MNRAS, 442, 900
Nanayakkara, T., Glazebrook, K., Kacprzak, G. G., et al. 2016, ApJ, 828, 21
—. 2017, MNRAS, 468, 3071
Ouchi, M., Mobasher, B., Shimasaku, K., et al. 2009, The Astrophysical Journal, 706, 1136
Papovich, C., Labbé, I., Quadri, R., et al. 2015, ApJ, 803, 26
Peebles, P. J. E. 1970, AJ, 75, 13
Persson, S. E., Murphy, D. C., Smee, S., et al. 2013, PASP, 125, 654
Reddy, N. A., Shapley, A. E., Sanders, R. L., et al. 2018, ApJ, 869, 92
Roberts-Borsani, G. W., Bouwens, R. J., Oesch, P. A., et al. 2016, ApJ, 823, 143
Robertson, B. E., Ellis, R. S., Furlanetto, S. R., & Dunlop, J. S. 2015, The Astrophysical Journal, 802, L19
Robertson, B. E., Furlanetto, S. R., Schneider, E., et al. 2013, ApJ, 768, 71
Salmon, B., Papovich, C., Finkelstein, S. L., et al. 2015, ApJ, 799, 183
Schmidt, M. 1959, ApJ, 129, 243
Scoville, N., Aussel, H., Brusa, M., et al. 2007, ApJS, 172, 1
Smit, R., Bouwens, R. J., Labbé, I., et al. 2014, ApJ, 784, 58
Spitler, L. R., Straatman, C. M. S., Labbé, I., et al. 2014, The Astrophysical Journal, 787, L36
Straatman, C. M. S., Spitler, L. R., Quadri, R. F., et al. 2016, ApJ, 830, 51
Straughn, A. N., Meurer, G. R., Pirzkal, N., et al. 2008, AJ, 135, 1624
Straughn, A. N., Pirzkal, N., Meurer, G. R., et al. 2009, AJ, 138, 1022
Strom, A. L., Steidel, C. C., Rudie, G. C., et al. 2017, ApJ, 836, 164
Tacconi, L. J., Neri, R., Genzel, R., et al. 2013, ApJ, 768, 74
Tang, M., Stark, D. P., Chevallard, J., & Charlot, S. 2019, MNRAS, 489, 2572
Tomczak, A. R., Quadri, R. F., Tran, K.-V. H., et al. 2016, ApJ, 817, 118
—. 2014, ApJ, 783, 85
Tran, K.-V. H., Alcorn, L. Y., Kacprzak, G. G., et al. 2017, ApJ, 834, 101
Tran, K.-V. H., Nanayakkara, T., Yuan, T., et al. 2015, ApJ, 811, 28
Trump, J. R., Sun, M., Zeimann, G. R., et al. 2015, ApJ, 811, 26
Trump, J. R., Konidaris, N. P., Barro, G., et al. 2013, ApJL, 763, L6
van der Wel, A., Bell, E. F., Häussler, B., et al. 2012, ApJS, 203, 24
van der Wel, A., Straughn, A. N., Rix, H.-W., et al. 2011, ApJ, 742, 111